AD_____

Award Number:
W81XWH-11-1-0070

TITLE:
Intraoperative Cerenkov Imaging for Guiding Breast
Cancer Surgery and Assessing Tumor Margins

PRINCIPAL INVESTIGATOR:
Guillem Pratx, PhD

CONTRACTING ORGANIZATION:
Leland Stanford Junior University
Stanford, CA 94305-2004

REPORT DATE:
December 2012

TYPE OF REPORT:
Annual Summary

PREPARED FOR:
U.S. Army Medical Research and Materiel Command
Fort Detrick, Maryland 21702-5012

DISTRIBUTION STATEMENT:
Approved for Public Release;
Distribution Unlimited

The views, opinions and/or findings contained in this report are those of the author(s)
and should not be construed as an official Department of the Army position, policy or
decision unless so designated by other documentation.

REPORT DOCUMENTATION PAGE

Form Approved
OMB No. 0704-0188

1. REPORT DATE	2. REPORT TYPE	3. DATES COVERED
December 2012	Annual Summary	01 December 2011–30 November 2012

4. TITLE AND SUBTITLE		5a. CONTRACT NUMBER
Intraoperative Cerenkov Imaging for Guiding Breast Cancer Surgery and Assessing Tumor Margins		
		5b. GRANT NUMBER
		W81XWH-11-1-0070
		5c. PROGRAM ELEMENT NUMBER
6. AUTHOR(S)		5d. PROJECT NUMBER
Guillem Pratx, PhD		5e. TASK NUMBER
		5f. WORK UNIT NUMBER
E-Mail: pratx@stanford.edu		

7. PERFORMING ORGANIZATION NAME(S) AND ADDRESS(ES)	8. PERFORMING ORGANIZATION REPORT NUMBER
The Leland Stanford Junior University Stanford, CA 94305	

9. SPONSORING / MONITORING AGENCY NAME(S) AND ADDRESS(ES)	10. SPONSOR/MONITOR'S ACRONYM(S)
U.S. Army Medical Research and Materiel Command Fort Detrick, Maryland 21702-5012	
	11. SPONSOR/MONITOR'S REPORT NUMBER(S)

12. DISTRIBUTION / AVAILABILITY STATEMENT

Approved for Public Release; Distribution Unlimited

13. SUPPLEMENTARY NOTES

14. ABSTRACT

Breast-conserving surgery is standard treatment for breast cancer. However, to be effective, the surgery must remove all malignant tissue. Currently, a significant fraction of BCS patients require additional re-excision surgery to remove residual cancer. This grant aims to develop a system to assess tumor margins during surgery, with the eventual goal of reducing re-excision surgery. This new technology should provide accurate information about the status of the margins in real-time, and therefore guide decision-making during surgery. The system can help surgeons decide when to stop the excision, and, if any, where to remove additional malignant tissue. It is hypothesized that the proposed approach, based on Cerenkov luminescence imaging, will help visualize malignant tissue directly in the operating room by exploiting the specificity of 18F-labeled fluorodeoxyglucose for malignant tissues.

15. SUBJECT TERMS

Breast cancer, surgery, imaging, Cerenkov luminescence

16. SECURITY CLASSIFICATION OF:			17. LIMITATION OF ABSTRACT	18. NUMBER OF PAGES	19a. NAME OF RESPONSIBLE PERSON USAMRMC
a. REPORT	b. ABSTRACT	c. THIS PAGE			
U	U	U	UU		19b. TELEPHONE NUMBER *(include area code)*

Table of Contents
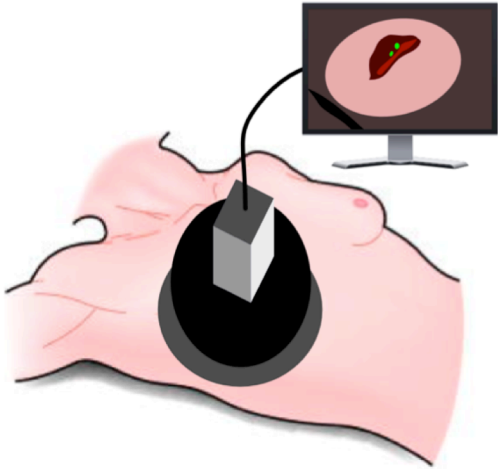
1. Introduction

Figure 1. Artistic rendering of the proposed approach. A Cerenkov luminescence imaging system is proposed for imaging the tumor margins and guide surgical resection.

Breast-conserving surgery (BCS) is standard treatment for breast cancer. However, to be effective, surgery must remove all malignant tissues. Currently, a significant fraction of BCS patients require additional re-excision surgery due to positive or close margins. This grant aims to develop a system to assess tumor margins during surgery, with the eventual goal of reducing re-excision surgery. This new technology should provide accurate information about the status of the margins in real-time, and therefore guide decision-making during surgery (**Fig. 1**). The system can help surgeons decide when to stop the excision, and, if any, where to remove additional malignant tissue. It is hypothesized that the proposed approach, based on Cerenkov luminescence imaging, will help visualize malignant tissue directly in the operating room. Cerenkov luminescence is the natural emission of visible light from radiotracers such as F18-fluorodeoxyglucose (FDG), a positron emission tomography (PET) radiotracer used to identify highly metabolic malignant tumors [1-3]. Since FDG is retained with high specificity by breast cancer tumors, it is hoped that Cerenkov luminescence imaging will provide a simple, sensitive, and inexpensive way to assess focal accumulations of FDG in the operating room, thereby allowing highly malignant tissues to be identified and resected.

2. Body

The second year of the funded project had the following accomplishments:

Task 3. In breast-tissue- and tumor-mimicking phantoms, characterize light and beta propagation and detection

While year 1 was focused on modeling of light diffusion using computer models, in year 2 we performed experiments intended to demonstrate Cerenkov luminescence imaging in breast-mimicking phantoms. We investigated several materials that have optical properties similar to breast tissue, and found the following mixture to have the best properties: 2% agarose for mechanical strength, 1% intralipd for optical scatter, 17 uM hemoglobin for optical absorption, and 15 mml NaN3 for antibiotic and antifungal properties. Using high-melt agarose, we first fabricated a cancerous lesion that contained 200 uCi of FDG. The mixture was poured in a 1 cm diameter spherical mold, which we fabricated as well. We let the mixture cool down and solidify. We then embedded the lesion in a hemispherical breast-shaped mold filled with low melt agarose. The cancerous lesion is therefore entirely surrounded by "normal" tissue. A color photograph of the phantom is shown in **Fig. 2A**.

We then placed the phantom in a custom Cerenkov imaging system. The system was built in Year 1 and was reported in the 2011 summary report. First, we took a Cerenkov luminescence image of the intact phantom. No Cerenkov signal was detectable because the lesion was too deep. After incision of the phantom, we were able to visualize strong Cerenkov signal emanating from the exposed lesion (**Fig. 2B**). We used this information to surgically remove a piece of phantom tissue, which we believed was the lesion. By taking another Cerenkov image, we were able to verify that the excised
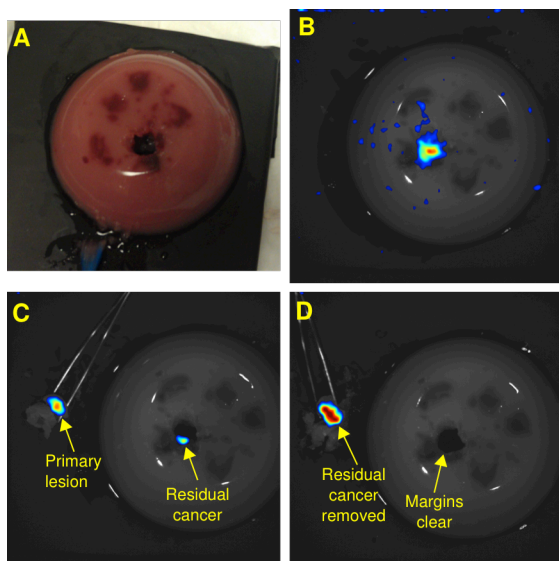
Figure 2. Simulation of breast cancer surgery guided by Cerenkov luminescence imaging using a phantom

sample was indeed malignant due to the high Cerenkov signal (**Fig. 2C**). We also found that the lesion resection had not been complete: there was significant luminescence coming from the tumor bed. We therefore performed a second resection, after which no further Cerenkov luminescence could be observed in the tumor bed (**Fig. 2D**). We then cut the phantom open to ensure that the entire lesion had been removed. Those experiments were repeated three times to ensure statistical significance.

This experiment helped show that Cerenkov luminescence imaging of FDG is a promising direction for guiding breast cancer surgery. However, we encountered a few difficulties. According to Dr Wapnir, an experienced breast surgeon who provided her expertise, the consistency and mechanical strength of the agarose-based phantoms was significantly different from human breast tissue. Furthermore, we noticed that some of the FDG was able to diffuse away from the primary lesion and into the surrounding matrix. FDG does not diffuse in vivo because it is retained within the cells. We will investigate other materials that have optical and mechanical similar to breast tissue. In the meantime, we will also report the experiments described here in a biomedical optics journal.

Task 4. Design algorithm for estimating signal depth based on combined spectral Cerenkov and beta scintillation imaging

We investigated penetration depth for Cerenkov imaging and direct beta detection with a scintillator. Overall, due to the positron range, direct beta detection with a scintillator was limited to sources of radiation less than 200 um deep. This makes direct beta detection most suitable for probing shallow tissues, such as residual cancer in the surgical field. Cerenkov luminescence was detected up to a depth of 5 mm (in tissue-mimicking material, given 100 uCi of activity).

We found that one of the advantages of the direct detection approach was that, due to the physics of scintillation, more photons were produced compared to Cerekonv luminescence. To quantify this effect, we measured the luminescence intensity using both methods (**Fig. 3A**) and found 30X stronger luminescence using a LSO scintillator.

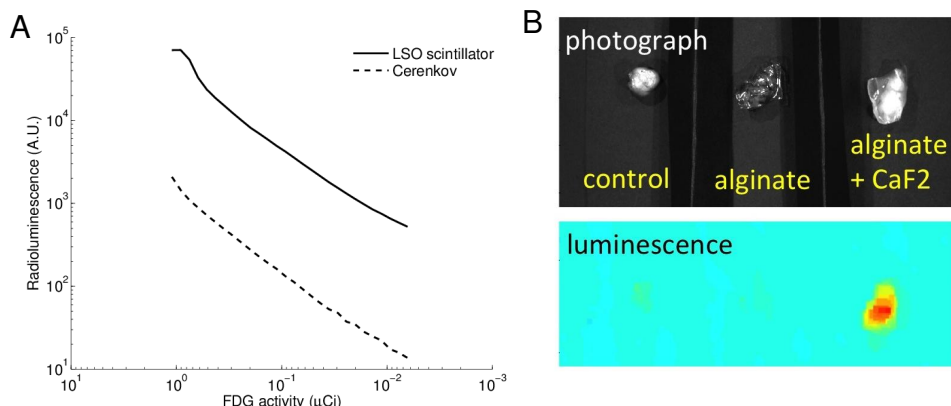**Figure 3.** (**A**) Luminescence intensity shown for Cerenkov luminescence and LSO scintillator. The scintillator provides ~30X signal enhancement. (**B**) Luminescence enhancement shown for a flexible scintillator film, applied directly on an excised tumor specimen.

This effect suggests that we can use a scintillator to amplify low concentrations of FDG in malignant

5

tissue. To this purpose, we fabricated thin, flexible alginate films that embed nano-sized scintillator powders (here, CaF2:Eu). To evaluate these scintillating films, we wrapped them around mouse xenograft tumors that were excised 1h after FDG injection. We found that the film lead to a 97% increase in luminescence intensity (Fig. 3B). We are planning to use these films to image FDG uptake in excised samples with higher sensitivity.

Task 5. Design algorithm for tomographic imaging of tracer distribution in a tissue sample from several projection, using the combined spectral Cerenkov and beta scintillation signal

In the past two years, several methods for performing Cerenkov tomographic reconstructions have been presented [1,2]. Since these algorithms are well adapted to the final goal of this project, we did not develop new reconstruction algorithms for tomographic reconstruction. We have evaluated one of these algorithms on phantom datasets and have achieved satisfying reconstructions.

Task 6. Determine the biodistribution of FDG in breast-cancer mouse xenografts at various time points, and correlate with Cerenkov imaging, autoradiography and pathology

In a preliminary study, we implanted two mice with MDA-MB-231 human xenografts. The mice were injected with FDG, and imaged using standard PET/CT (**Fig. 4A**). After euthanasia, the mice were imaged with Cerenkov luminescence before and after excision of the tumors (**Fig. 4B**). The specimens were frozen and sectioned, then imaged with standard autoradiography (**Fig. 4C**). Last, slices from the same specimen were also imaged using the high-spatial-resolution imaging system (called radioluminescence microscope) developed in year 1 of this project. A full report on this imaging system was recently published [6] and is attached in the Appendix (attachment 1). The results of this experiment suggest that Cerenkov luminescence is best adapted for surveying the surgical field, because it allows the visualization of a large area (e.g. **Fig. 1**). The radioluminescence microscope is more suitable to analyzing small excised specimen with high spatial resolution. It can simultaneously visualize radionuclide probe distribution and tissue morphology for accurate assessment of tumor margins with very high spatial resolution. FDG uptake in single cancer cells can be visualized to ensure that the outer rim of tissue on the excised specimen (i.e. the margin) is cancer-free.

In year 2 of this project, we have also developed a new image acquisition method for the radioluminescence microscope system that is more accurate. Rather than using a long exposure (e.g. 5 min), the new method takes thousands of images, each with a short exposure (e.g. 100 ms). This allows single molecules of FDG to be visualized as they decay. This particle counting scheme has two advantages: (1) the spatial resolution is improved because each individual radioactive decay event can be localized with greater precision; and (2) the images have higher quantitative accuracy because each decay event is counted as "one" and not a random quantity. This new imaging scheme was described in a new journal article submitted to
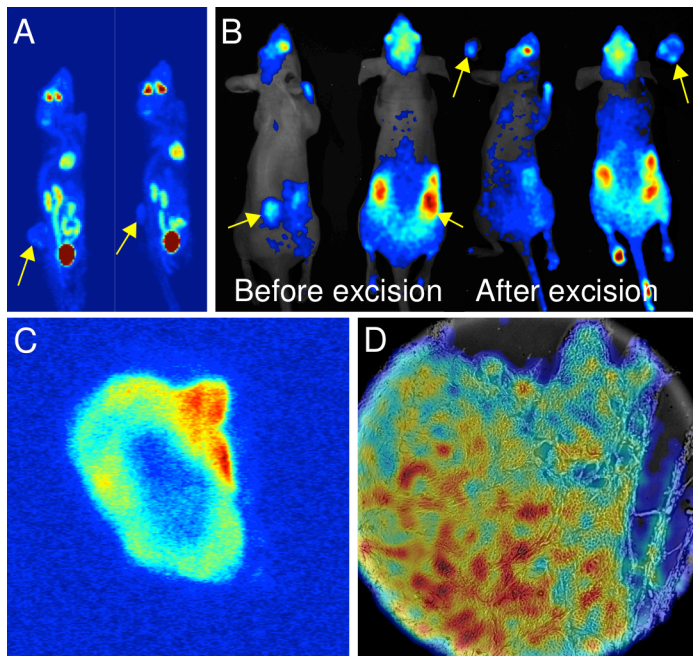

Figure 4. Multimodal imaging of two mice bearing MDA-MB-231 xenograft tumors. (**A**) PET/CT imaging; (**B**) Cerenkov luminescence imaging; (**C**) Autoradiography; and (**D**) Radioluminescence microscopy. Arrows show the two tumors.

the Journal of Nuclear Medicine, and is currently undergoing a second round of peer-review. The article will be submitted to the BCRP program once published, with next year's report.

In order to further study Cerenkov luminescence imaging in an in vivo system, we developed murine models of human cancer. We selected a C6 glioma cancer model for this study because cancer xenografts based on this model are more infiltrative and more representative of actual breast cancer, at least from a physical perspective. The C6 glioma model is more likely to result in residual cancer after surgery, which makes it an ideal model for evaluating Cerenkov luminescence imaging. Furthermore, we developed an endoscopic Cerenkov imaging system that is more applicable to translation to human imaging. This system includes a fiber bundle to visualize Cerenkov luminescence signal at various body sites (including inside cavities such as the gastrointestinal tract). We were the first group to report the possibility of imaging Cerenkov luminescence through an endoscopic device. This system and the results of this study are attached in the appendix (attachment 3).

Training: As part of the comprehensive training plan, I have attended various events to increase my knowledge of breast cancer research. I have attended the 2012 Personalized Medicine World Conference, during which were presented several new targeted therapies for breast cancer, and the World Molecular Imaging Conference, which presented several new imaging probes for breast cancer. I also frequently attend on-campus events related to imaging and/or breast cancer, such as the MIPS seminar series, the Nanobio talks, the Radiology Grand Rounds, as well as the residents lecture series in Radiation Oncology. I regularly meet with both my mentor and co-mentor to discuss research progress. Over the summer, I have also taught a class on mechatronics system to develop skills important for my future faculty career.

3. Key Research Accomplishments

- Phantom study simulating breast cancer surgery guided by Cerenkov luminescence imaging
- Investigation of Cerenkov imaging at different depths
- New method developed to image single radionuclide decay events with cellular resolution, resulting higher image quality and accuracy for radioluminescence microscopy
- First demonstration of radioluminescence microscopy for tissue samples, such as tumor specimen excised during breast cancer surgery
- Imaging of breast cancer xenograft models using multiple modalities: PET/CT, Cerenkov luminescence imaging, autoradiography, and radioluminescence microscopy

4. Reportable Outcomes

- Two journal article published, one currently under review

  Pratx G, Chen K, Sun C, Martin L, Carpenter CM, Olcott PD & Xing L, "Radioluminescence microscopy: Measuring the heterogeneous uptake of radiotracers in single living cells", *PLOS One* 7(10), e46285 (2012)

  Liu HG, Carpenter CM, Jiang H, **Pratx G**, Sun C, Buchin MP, Gambhir SS, Xing L, & Cheng Z, "Intraoperative imaging of tumors using Cerenkov luminescence endoscopy: A Feasibility Experimental Study", *J. Nucl. Med.* 53(10), pp. 1579-1584 (2012)

G. Pratx, K. Chen, C. Sun, C. Carpenter, & L. Xing, "High-resolution radioluminescence microscopy of FDG uptake by reconstructing the beta ionization track", *J. Nucl. Med.*, under second review

- One conference presentation (Oral)

  Pratx G, Chen K, Sun C, Martin LM, Carpenter CM & Xing L, "A new method to measure radiotracer uptake in single living cells", oral presentation, WMIC, 2012

  Selected as a Young Investigator Award semi-finalist

- One US patent application

  Imaging the Heterogeneous Uptake of Radiolabeled Molecules in Single Living Cells, US patent application, 13/492,606

- One travel award to attend WMIC in Dublin (2012)
- One class taught (Mechatronics system)

5. Conclusions

In the second year of this postdoctoral award, we have further refined instrumentation designed to image FDG uptake during breast cancer surgery. The strategy for assessing residual disease during breast surgery consists of three steps: before surgery, standard PET/CT is used to evaluate how extensive the disease is, based on the distribution. Then, during surgery, Cerenkov luminescence is used to survey the tumor bed and assess the presence of residual disease. Last, the surface of the excised specimen is imaged with radioluminescence microscopy, which has the ability to visualize a single malignant cell. The proposed approach will therefore provide real-time assessment of the disease extent at different stages of breast-conserving surgery, i.e. before, during, and after resection of the primary tumor. This multimodal strategy was demonstrated for a phantom study as wall as for a murine breast cancer xenograft model.

6. References

[1] Cherenkov, Pavel A. (1934). "Visible emission of clean liquids by action of γ radiation". *Doklady Akademii Nauk SSSR* 2:451

[2] Ross HH, "Measurement of beta-emitting nuclides using Cerenkov radiation", *Analytical Chemistry* 41 (10) pp. 1260-1265, 1969

[3] R Robertson, M S Germanos, C Li, G S Mitchell, S R Cherry and M D Silva, "Optical imaging of Cerenkov light generation from positron-emitting radiotracers", *Phys. Med. Biol.* 54 pp. N355, 2009

[4] C. Li, G. Mitchell, and S. Cherry, "Cerenkov luminescence tomography for small-animal imaging," *Opt. Lett.* 35, 1109-1111 (2010).

[5] Z. Hu, J. Liang, W. Yang, W. Fan, C. Li, X. Ma, X. Chen, X. Ma, X. Li, X. Qu, J. Wang, F. Cao, and J. Tian, "Experimental Cerenkov luminescence tomography of the mouse model with SPECT imaging validation," *Opt. Express* 18, 24441-24450 (2010).

[6] **Pratx G**, Chen K, Sun C, Martin L, Carpenter CM, Olcott PD & Xing L, "Radioluminescence microscopy: Measuring the heterogeneous uptake of radiotracers in single living cells", *PLOS One* 7(10), e46285 (2012)

[7] Liu HG, Carpenter CM, Jiang H, **Pratx G**, Sun C, Buchin MP, Gambhir SS, Xing L, & Cheng Z, "Intraoperative imaging of tumors using Cerenkov luminescence endoscopy: A Feasibility Experimental Study", *J. Nucl. Med.* 53(10), pp. 1579-1584 (2012)

7. Appendices

Attachment 1: **Pratx G**, Chen K, Sun C, Martin L, Carpenter CM, Olcott PD & Xing L, "Radioluminescence microscopy: Measuring the heterogeneous uptake of radiotracers in single living cells", *PLOS One* 7(10), e46285 (2012)

Attachment 2: Liu HG, Carpenter CM, Jiang H, **Pratx G**, Sun C, Buchin MP, Gambhir SS, Xing L, & Cheng Z, "Intraoperative imaging of tumors using Cerenkov luminescence endoscopy: A Feasibility Experimental Study", *J. Nucl. Med.* 53(10), pp. 1579-1584 (2012)

Radioluminescence Microscopy: Measuring the Heterogeneous Uptake of Radiotracers in Single Living Cells

Guillem Pratx[1]*, Kai Chen[1], Conroy Sun[1], Lynn Martin[1], Colin M. Carpenter[1], Peter D. Olcott[2], Lei Xing[1]

1 Department of Radiation Oncology, Stanford University School of Medicine, Stanford, California, United States of America, **2** Department of Radiology, Stanford University School of Medicine, Stanford, California, United States of America

Abstract

Radiotracers play an important role in interrogating molecular processes both *in vitro* and *in vivo*. However, current methods are limited to measuring average radiotracer uptake in large cell populations and, as a result, lack the ability to quantify cell-to-cell variations. Here we apply a new technique, termed *radioluminescence microscopy*, to visualize radiotracer uptake in single living cells, in a standard fluorescence microscopy environment. In this technique, live cells are cultured sparsely on a thin scintillator plate and incubated with a radiotracer. Light produced following beta decay is measured using a highly sensitive microscope. Radioluminescence microscopy revealed strong heterogeneity in the uptake of [18F]fluoro-deoxyglucose (FDG) in single cells, which was found consistent with fluorescence imaging of a glucose analog. We also verified that dynamic uptake of FDG in single cells followed the standard two-tissue compartmental model. Last, we transfected cells with a fusion PET/fluorescence reporter gene and found that uptake of FHBG (a PET radiotracer for transgene expression) coincided with expression of the fluorescent protein. Together, these results indicate that radioluminescence microscopy can visualize radiotracer uptake with single-cell resolution, which may find a use in the precise characterization of radiotracers.

Introduction

The use of radiotracers to probe biological processes has several advantages over other approaches: radiotracers can be synthesized with chemical composition nearly identical as a given compound of interest; their concentration measured with exquisite sensitivity [1]; and their distribution imaged in vivo with positron emission tomography (PET) or single photon emission computer tomography (SPECT) [2,3,4,5]. With the widespread use of radionuclide imaging in research and in hospitals, we need to better understand how properties specific to individual cells (e.g. gene expression, cell cycle, cell damage, and cell morphology) affect the uptake and retention of radiotracers. In particular, disease and therapy can alter cellular mechanisms in a heterogeneous manner; how these alterations affect radiotracer uptake at the single-cell level is currently unknown and of critical importance.

The averaging effect of measuring radiotracer uptake in pooled cell populations can mask important differences between cells belonging to the same population. However, current approaches lack the ability to distinguish radiotracer uptake in individual living cells. For instance, film autoradiographs can be examined with light [6] or electron microscopy [7] to visualize radioactive decay within individual cells but the method is limited to fixed tissues and low energy radionuclides (e.g. 14C and 3H). Digital autoradiography techniques (e.g. storage phosphor [8], electronic detection [9,10], thin phosphor layer [11], scintillator [12], and gaseous

chamber [13]) offer higher detection efficiency and dynamic range but poorer spatial resolution (>30 μm), insufficient to resolve individual cells. Likewise, *in vivo* radiotracer imaging and scintillation counting can only measure signals from large cell populations.

Here a new method, termed radioluminescence microscopy, is proposed to measure radiotracer uptake in single living cells. Radioluminescence is the physical process by which ionizing charged particles produce light in certain materials. Due to the short range of beta particles (electrons or positrons), radioluminescence occurs near the location of the radioactive emitter. The range of these particles is further reduced in dense, high-atomic-number materials such as inorganic scintillators. Following this observation, we hypothesized that the radioactivity of single cells could be measured by placing these cells in contact with a scintillator plate and imaging the resulting optical signal using a sensitive microscope with high numerical aperture (NA) and high photon sensitivity. Furthermore, we envisioned that this technique could be applied concurrently with standard fluorescence microscopy because scintillator materials are optically clear in the visible range.

The proposed radioluminescence microscopy set-up consists of a 100 μm-thin CdWO$_4$ scintillator plate, on which cells have adhered, immersed in a glass-bottom dish filled with cell culture medium (**Figure 1A&B**). The dish is imaged using an inverted
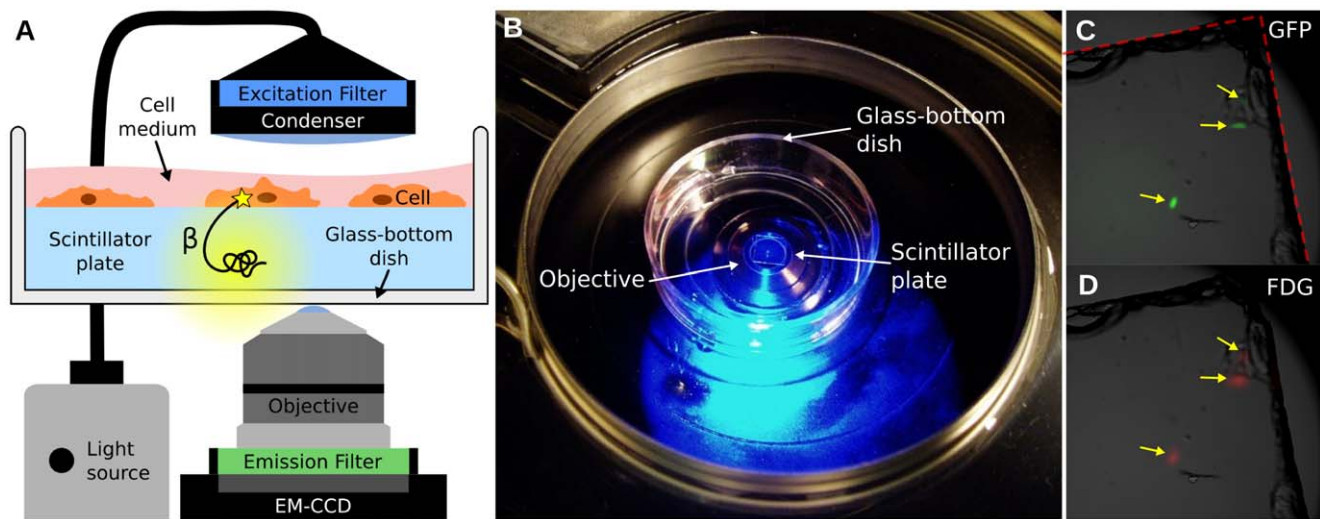
Figure 1. Overview of the radioluminescence microscope. (**A**) Radioluminescence is produced within a scintillator plate following the emission of a beta particle from a radiotracer within a cell (yellow glow). The optical photons are captured by a high-numerical-aperture objective coupled to a deep-cooled EM-CCD camera. Emission and excitation filters used in combination with a light source allow for concurrent fluorescence and brightfield microscopy. (**B**) Photograph of the system showing a glass-bottom dish containing a scintillator plate immersed in cell culture medium and placed into the inverted microscope. (**C**) Three GFP-expressing HeLa cells located near the corner of a scintillator plate were localized using fluorescence microscopy (*arrows*). The edge of the scintillator plate is outlined in red. (**D**) After incubation with FDG (400 μCi, 1 h), these three cells also produced focal radioluminescence signal coincident with the fluorescent emission.
doi:10.1371/journal.pone.0046285.g001

microscope fitted with a high-NA objective and an electron-multiplying charge-coupled device (EM-CCD).

As an illustration of the methods, human ovarian cancer cells (HeLa) expressing the green fluorescent protein (GFP) were imaged after incubation with [18F]fluorodeoxyglucose (FDG; 400 μCi). Three isolated cells were localized near the corner of a scintillator plate, which is clearly visible on the brightfield micrograph (**Figure 1C**, *dashed red line*). Both fluorescence and radioluminescence images displayed focal signal at the locations of the three cells (arrows, **Figure 1C&D**).

Results

Radioluminescence Imaging of FDG uptake in Single Cells

FDG is preferentially taken up and retained within tissues with high glucose metabolism such as malignant tumors [14,15,16]. Measuring FDG uptake in a heterogeneous cell population is of great interest as it may help better understand the heterogeneous metabolic alterations displayed by tumors, and the impact that the tumor microenvironment has on these alterations [17,18]. However, there does not exist a standard method for measuring radiotracer uptake at the single cell level. Therefore, to validate the use of radioluminescence microscopy for FDG imaging, we used a fluorescent glucose analog as a surrogate for FDG uptake in single cells.

After a 1 h glucose fasting period, we incubated human breast cancer cells (MDA-MB-231) for 1 h at 37°C with FDG (400 μCi) and 2-[N-(7-nitrobenz-2-oxa-1,3-diaxol-4-yl)amino]-2-deoxyglucose (2-NBDG; 100 μM) [19,20]. After washing the cells, we acquired brightfield, radioluminescence and fluorescence micrographs. We observed good co-localization between the radioluminescence intensity and the cell outline seen on brightfield images (**Figure 2A**). Furthermore, the radioluminescence intensity varied significantly from cell to cell, indicating heterogeneous uptake of FDG. The single-cell radioluminescence signal was correlated with

2-NBDG fluorescence (**Figure 2B**, $p < 10^{-5}$, $r = 0.74$). An exact correlation between FDG and 2-NBDG is not expected due to (i) possibly distinct transport mechanisms [21]; and (ii) the inability of 2-NBDG to fluoresce after being metabolized [22]. A line profile through the fluorescence and radioluminescence images confirms co-localization of FDG and 2-NBDG signals (**Figure 2C**).

Pharmacokinetic Analysis of FDG Metabolism in Single Cells

The transport and retention of FDG in a cell is influenced by multiple factors, such as the expression of various genes, the density of glucose transporters on the cell surface, the cell size, and the levels and activities of hexokinase and phosphatase enzymes [15]. Under steady-state conditions, the intracellular and extracellular FDG concentrations are in equilibrium. However, rapid changes in the extracellular environment induce a transient response characteristic of the cell's glucose metabolism parameters. These parameters can be estimated using pharmacokinetic modeling techniques. The ability to manipulate a cell's environment is unique to an *in vitro* setting and cannot be easily replicated *in vivo*. Furthermore, pharmacokinetic modeling from PET or gamma counting measurements requires assumptions such as uniform radiotracer concentration and homogeneous rate parameters for each compartment [23]. These assumptions may not be satisfied in practice because each cell in the compartment is characterized by unique parameters. Pharmacokinetic modeling at the single-cell level may provide more optimal characterization of cellular parameters.

To investigate the utility of radioluminescence microscopy for single-cell pharmacokinetic studies, we monitored the uptake of FDG in breast cancer cells (MDA-MB-231) over 8 h. After depriving cells of glucose for 1 h, we added FDG (5 μCi) to their medium and acquired serial brightfield and radioluminescence images every 6 min for 8 h (**Figure 3A** & **Video S1**). Although FDG uptake varied significantly from cell to cell, all cells displayed
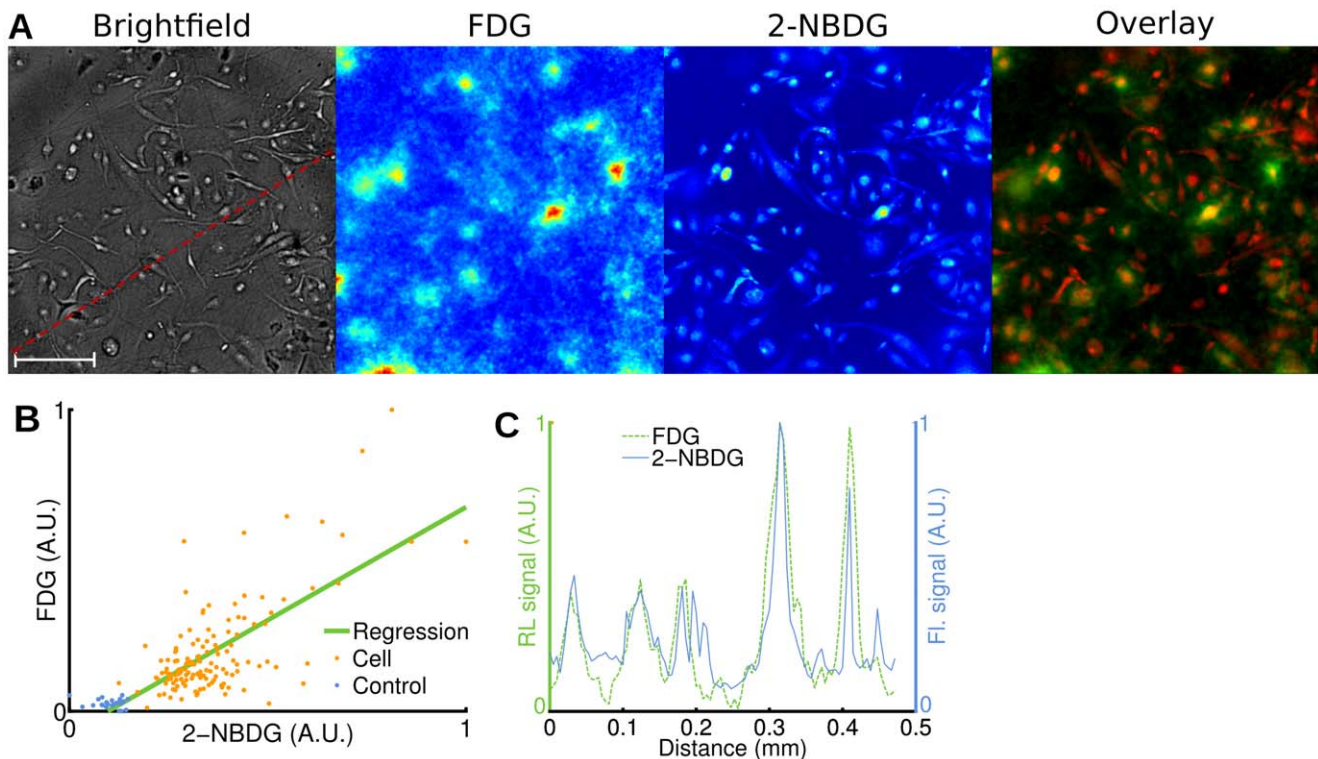
Figure 2. Radioluminescence imaging of FDG uptake in single cells. Human breast cancer cells (MDA-MB-231) were deprived of glucose for 1 h, incubated for 1 h with FDG (400 µCi) and 2-NBDG (100 µM), and then washed. (**A**) Brightfield (scale bar, 100 µm.), radioluminescence (FDG), and fluorescence (2-NBDG) micrographs (Objective: 40X/1.3 NA). Overlay, showing co-localized radioluminescence (green) and fluorescence (red). (**B**) Scatter plot comparing FDG and 2-NBDG uptake, computed over 140 cells (light red dots) and 26 control ROIs (blue dots). The green line was obtained by linear regression (correlation, r = 0.74). Arbitrary units (A.U.). (**C**) Radioluminescence (FDG) and fluorescence (2-NBDG) intensity shown along a line profile [red dashed line in (A)].
doi:10.1371/journal.pone.0046285.g002

the same linear increase in radioactivity, followed by a plateau and a slow decrease after 3 h (**Figure 3D**).

We performed two other sets of experiment to highlight efflux of FDG from a cell. Toward this goal, we next subjected breast cancer cells (MDA-MB-231) to conditions known to minimize FDG influx, i.e. competition from glucose (**Figure 3B** & **Video S2**) and withdrawal of FDG (**Figure 3C** & **Video S3**). The addition of glucose to the medium (25 mM) at 2 h lead to a strong decline in cell radioactivity (**Figure 3E**) as FDG and glucose competed for the same glucose transporters. Withdrawing FDG from the media of cells that had previously been incubated with FDG (400 µCi, 1 h) also resulted in a similarly fast decrease in cell radioactivity (**Figure 3F**).

The uptake and metabolism of FDG can be mathematically modeled using a two-tissue compartmental model (**Figure 4A**), whose rate constants K_1, k_2, k_3 and k_4 represent the influx, efflux, phosphorylation, and dephosphorylation of FDG, respectively. Influx of FDG in cells (as shown in **Figure 3A**) was quantified by Patlak analysis. Single-cell time-activity curves measured by radioluminescence microscopy were found consistent with Patlak's model, at least in the early time points: After a short transient period, equilibrium was established and the intracellular concentration of FDG increased linearly with time due to the irreversible trapping of FDG into the cell (e.g. **Figure 4B**). The slope of the linear rise is the product of two terms, namely K_1, the influx rate, and $k_3/(k_2+k_3)$, the fraction of the intracellular FDG irreversibly metabolized.

We found large variations in the Patlak coefficients across the cells that were imaged, indicating that seemingly identical cells process glucose heterogeneously. Furthermore, solving for the pharmacokinetic coefficients K_1, k_2 and k_3 showed that K_1 (influx) and k_2 (efflux) were correlated ($p < 10^{-5}$, $r = 0.89$, **Figure 4C**) but K_1 and k_3 (phosphorylation) were not ($p = 0.6$, $r = -0.08$, **Figure 4D**). Also, the majority of cells stopped accumulating FDG at approximately 3 h and a slow decrease in cell FDG concentration was observed (**Figure 3D**). The non-negligible rate of FDG dephosphorylation (k_4) is likely the main factor contributing to that effect. However, dephosphorylation alone should result in the FDG concentration reaching a steady plateau due to equilibration of phosphorylation and dephosphorylation. The slow decrease that was observed instead may have been caused by increased competition from unlabeled 2DG (a byproduct of FDG synthesis) as FDG concentration diminished due to radioactive decay.

We also derived a mathematical model to represent FDG efflux from a cell after withdrawal of FDG (as shown in **Figure 3C**), composed of the sum of a slow and a fast exponential decay. The model was found to be in agreement with radioluminescence measurements of single cells (e.g. **Figure 4E**), confirming that two processes are occurring concurrently at different rates. The first process describes the rapid diffusion of unbound FDG out of the cell (rate λ_1), whereas the second process involves the slow dephosphorylation of FDG-6-phosphate (rate λ_2). While the efflux rate was heterogeneous over the cell population studied, we found
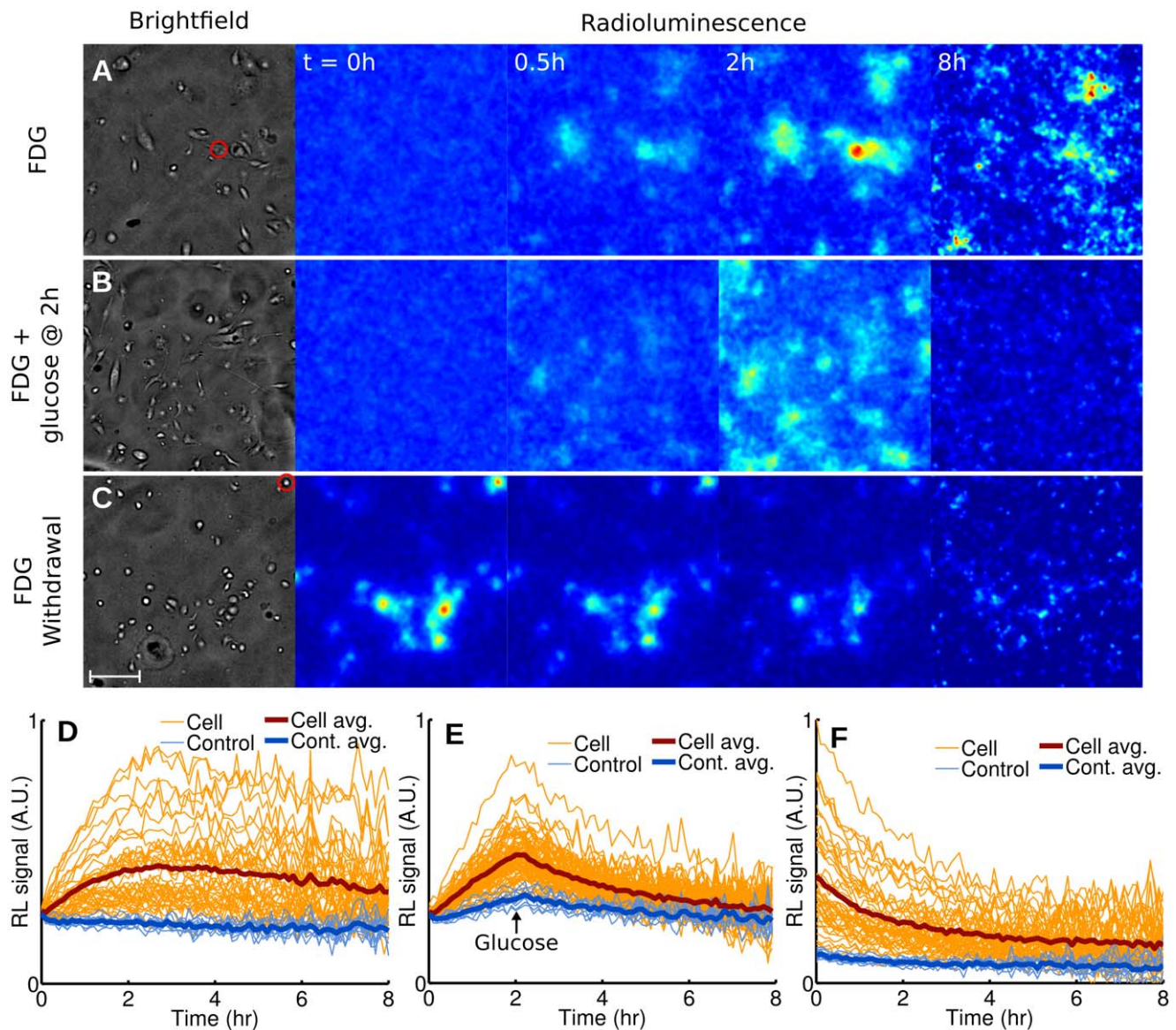
Figure 3. Dynamic radioluminescence imaging of FDG in single cells. Micrographs (brightfield and radioluminescence) were acquired every 6 min for 8 h for three experiments. (**A**) MDA-MB-231 cells are imaged while being incubated with FDG (5 µCi). (**B**) Glucose (25 mM) is added 2 h after the beginning of the incubation with FDG (5 µCi). (**C**) FDG is withdrawn at the start of imaging after incubation (1 h, 400 µCi). Scale bar: 100 µm. (**E–F**) Time-activity curves plotted for individual cells (light red lines) and 10 control ROIs manually selected in the background (light blue lines), for all three experiments. The thick red and blue lines represent the average for cells and control ROIs, respectively.
doi:10.1371/journal.pone.0046285.g003

no significant correlation between the fast and slow components of the decay ($p = 0.9$, $r = -0.02$, **Figure 4F**).

Single-cell Characterization of Transgene Expression with a PET Probe

To further validate radioluminescence microscopy, we investigated the uptake of 9-(4-[18F]Fluoro-3-hydroxymethylbutyl)-guanine (FHBG) in cancer cells that were heterogeneously transfected to express the mutant herpes simplex virus type 1 truncated thymidine kinase (HSV1-ttk). HSV1-ttk can selectively metabolize and trap radiolabeled substrates such as FHBG [24]. Because FHBG has low affinity for mammalian thymidine kinases (TK) and high affinity for viral HSV1-TK, it can be used to image cell trafficking in living subjects with PET [25]. To assess the

expression of the HSV1-ttk transgene with fluorescence microscopy, we built a fusion reporter that also encodes the monomeric red fluorescent protein 1 (mrfp1).

We transfected human cervical cancer cells (HeLa) with the fusion reporter vector encoding HSV1-ttk and mrfp1. Radioluminescence microscopy of FHBG (incubation 2h with 300 µCi) demonstrated focal radiotracer uptake, with individual cells clearly resolvable under 100X magnification (**Figure 5A**). Using fluorescence microscopy, we estimated that 88% of the cells (217/245) had been successfully transfected with the fusion transgene. All of those cells were also clearly distinguishable on the radioluminescence fluorescence image (**Figure 5B**). We also found that 9% of the cells (21/245) had not been transfected and did not produce any fluorescence. These cells did not present a radioluminescence signal, which suggest that they did not retain FHBG. The
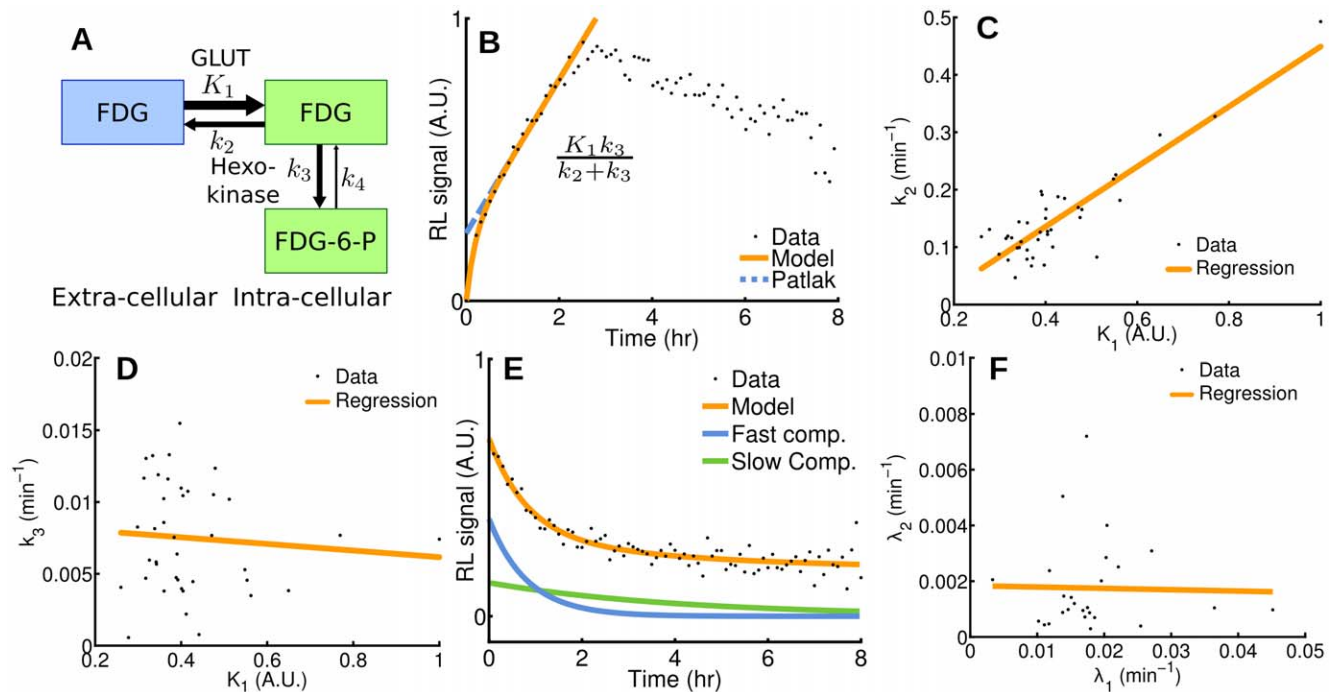
Figure 4. Pharmacokinetics analysis in single cells. (**A**) Two-tissue compartmental model describing FDG pharmacokinetics, including influx (K_1), efflux (k_2), phosphorylation to FDG-6-phosphate (k_3), and dephosphorylation (k_4). (**B**) Patlak analysis modeling FDG influx kinetics for a single cell (highlighted by a red circle in Figure 3A). (**C,D**) Rate of efflux (k_2) and phosphorylation (k_3) plotted as a function of rate of influx (K_1) for all the cells in the microscope's field of view. (**E**) Compartmental analysis modeling FDG efflux kinetics from a single cell (highlighted by a red circle in Figure 3C) after withdrawal of FDG, presenting a fast and a slow component. (**F**) The model for FDG efflux is the sum of a fast and a slow component (rates λ_1 and λ_2, respectively), which are plotted for all the cells in the field of view.
doi:10.1371/journal.pone.0046285.g004

remaining 5% of the cells (7/245) were excluded from the analysis due to ambiguous radioluminescence intensity, mostly due to the proximity of one or more strongly positive cells (e.g. **Figure 5B**, green arrow). Generally, in our system, radioluminescence signals for FHGB-positive and negative cells were more distinctly separated than fluorescence signals for RFP-positive and negative cells (**Figure 5B**, white arrows). A line profile passing through four cells showed good co-localization of RFP and FHBG (**Figure 5D**).

While uptake of FHBG was coincident with RFP fluorescence, fluorescence intensity was not strongly predictive of radioluminescence intensity (**Figure 5C**; correlation, $r = 0.34$), indicating that although the HSV1-tk reporter gene expression is required for FHBG uptake, the level of transgene expression is not solely responsible for the extent of FHBG uptake. In a separate experiment, the FHBG substrate displayed no affinity for mammalian TK enzyme: wild-type HeLa cells incubated with FHBG (300 µCi, 2h) showed no measureable radioluminescence signal (**Figure 5E**).

Performance Characterization

To investigate the spatial resolution of the imaging set-up, dry FDG aggregates were imaged with the radioluminescence microscope. Brightfield and radioluminescence images displayed good correlation ($r = -0.79$, $p < 10^{-5}$; **Figure 6A–G**). From these measurements, we estimated the microscope spatial resolution to be 5 µm (full-width half-maximum).

The sensitivity of the microscope was measured by imaging the decay of a uniform distribution of FDG (2.6 µCi initially) over 24 hours. The average pixel intensity (expressed as a percentage of the pixel intensity in the first frame) decreased exponentially with time with a half-life consistent with the decay of ^{18}F (**Figure 6H**).

The relationship between the average pixel intensity and the average activity per area remained linear all the way down to approximately 0.1 fCi/µm^2. The signal-to-noise ratio (SNR) also decreased with decreasing activity (**Figure 6I**). To visualize image features, a SNR of at least five is required (Rose criterion [26]), which corresponds to a minimum activity area density of 4 fCi/µm^2. This is equivalent to 1.4 molecules of FDG per µm^2.

Discussion

For the first time, radioluminescence microscopy enables the quantification of radiotracer uptake and pharmacokinetics at the single-cell level. Because a similar method does not currently exist, we validated the new approach by comparing single-cell radiotracer measurements against surrogate quantities. Hence, we found FDG uptake to be consistent with fluorescence imaging of a glucose analog (**Figure 2**), with pharmacokinetics characteristic of a two-tissue compartmental model (**Figure 3** and **Figure 4**). Furthermore, in a cell population heterogeneously transfected with a fusion PET/fluorescence reporter, we verified that FHBG uptake was concordant with fluorescence imaging of mrfp1 (**Fig. 5**).

Although radioluminescence microscopy is not yet capable of visualizing intracellular radiotracer distributions, it can measure the radioactivity of single cells provided that those cells are spatially separated on the scintillator plate. Accurate measurements can be achieved with cell-to-cell separation of 10 µm or more. Radioluminescence micrographs can be acquired in 5 min or less using mostly off-the-shelf instrumentation. Commonly used beta emitters such as ^{18}F, ^{131}I, and ^{64}Cu can be used to produce such images.
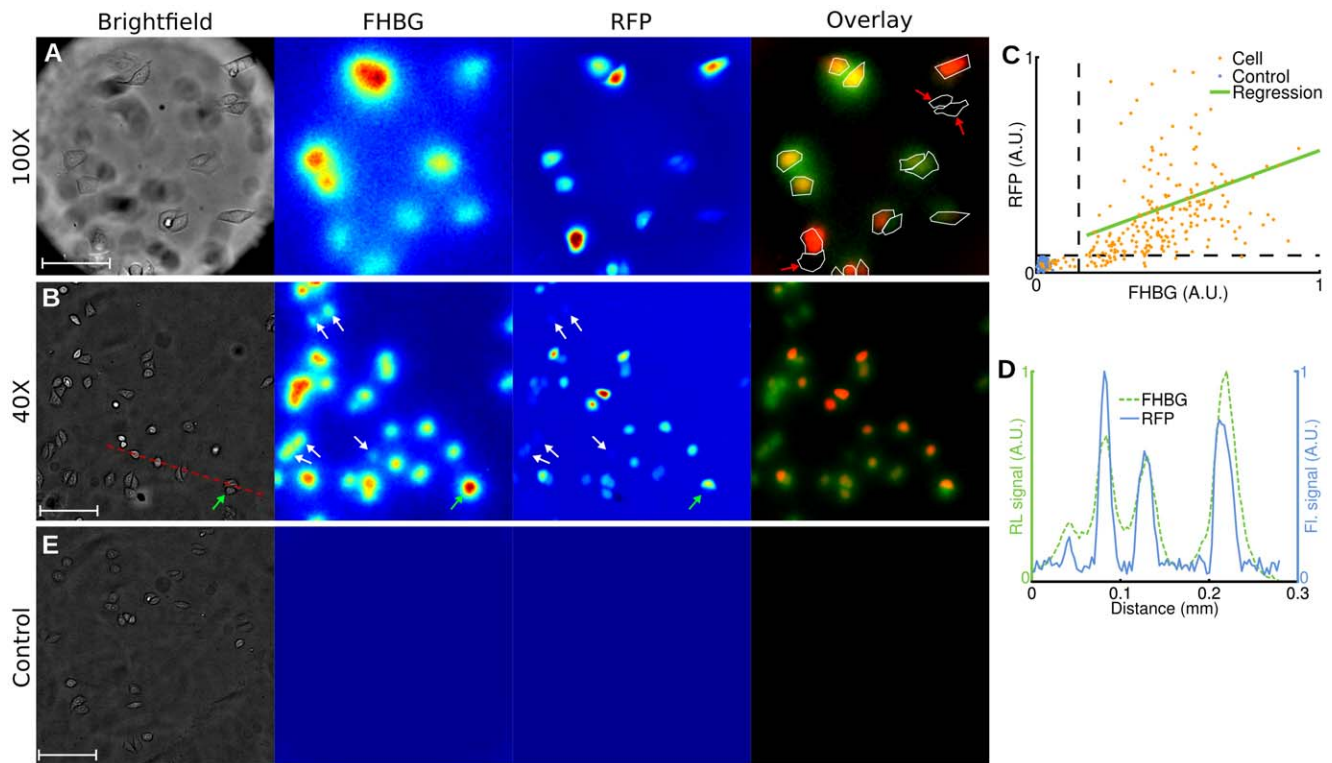
Figure 5. Radioluminescence imaging of gene expression in single cells. Human cervical cancer cells (HeLa) transfected with a fusion PET/fluorescence reporter gene were incubated with FHBG (300 µCi, 2 h). (**A**) Brightfield (scale bar, 50 µm), radioluminescence (FHBG), and fluorescence (RFP) micrographs (objective, 100X/1.35 NA). Overlay shows FHBG radioluminescence (green), RFP fluorescence (red), and cell outline segmented from brightfield. Cells negative for RFP are also negative for FHBG (red arrows). (**B**) Same as (A), but with a 40X/1.3 NA objective (scale bar, 100 µm). White arrows indicate cells with weak fluorescence intensity but substantial radioluminescence intensity. The green arrow points to a cell with no RFP expression but ambiguous radioluminescence intensity. (**C**) Scatter plot of FHBG vs. RFP uptake, computed for 245 cells (light red dots) and 100 control ROIs (blue dots). Arbitrary units. (**D**) Radioluminescence and fluorescence shown along a line profile [red dashed line in (A)]. (**E**) Same experiment as (A,B), but using control wild-type HeLa cells (scale bar, 100 µm).
doi:10.1371/journal.pone.0046285.g005

While radioluminescence microscopy is mainly intended to image tissue culture cells, the method may be applicable to imaging solid tissue sections. However, in the current configuration, it may not provide single-cell resolution for dense tissue section. One solution to this problem is to dissociate the tissue prior to imaging to ensure sufficient separation between cells [27]. We are also currently investigating several approaches to further improve the spatial resolution of the system.

We expect that radioluminescence microscopy will become a useful technique for the precise characterization of radiotracer uptake and pharmacokinetics at the single-cell level. New developments in scintillator research will undoubtedly improve the performance of the technique. Thinner scintillator plates with higher density and light yield will provide better spatial resolution and signal-to-noise ratio. Progress in image processing and calibration techniques will also allow for more quantitative measurements of radiotracer concentration in single cells.

Materials and Methods

Microscopy Set-up

Adherent cancer cells were seeded sparsely on 5 mm × 5 mm × 0.1 mm plates made of $CdWO_4$, a non-hygroscopic inorganic scintillator, with both sides polished (Figure 1A). $CdWO_4$ has relatively high light yield (12,000–15,000 photon/MeV), high effective atomic number ($Z_{eff} = 64$), high density (7.9 g/cm^3), and no significant afterglow. The scintillator plates, loaded with cells,

were placed in microscopy dishes (#0 cover glass, 0.085–0.115 mm, In Vitro Scientific) filled with fresh media (**Figure 1A&B**). The use of thin scintillator plates and thin-bottom imaging dishes is required to accommodate the short working distance of the microscope objective (200 µm).

The imaging dishes were placed in a bioluminescence microscope (LV200, Olympus) outfitted with either a 40X/1.3 NA oil objective (UPLFLN40XO, Olympus) or a 100X/1.35 NA oil objective (UPLAPO00XOI3, Olympus), and a deep-cooled electron-multiplying charge-coupled device (EM-CCD; ImageEM C9100-14, Hamamatsu) (**Figure 1 A&B**). The C9100-14 CCD is a back-thinned frame transfer device, with a 1024×1024 array of 13 µm×13 µm pixels. The LV200 is also equipped with temperature, humidity, and CO_2 regulation for extended live cell imaging.

Brightfield images were acquired with no EM gain, a neutral-density filter on the excitation, and the emission shutter open. For the 40X magnification, radioluminescence images were taken with an exposure time of 5 min, an EM gain of 251/1200, 2×2 pixel binning, the excitation shutter closed, and the emission shutter open. For the 100X magnification, the exposure time was 20 min and the EM gain 505/1200. We used the brightfield mode to set the microscope into focus. Optimal radioluminescence focus was achieved when the cells displayed sharp positive contrast in the corresponding brightfield image. For fluorescence microscopy, we used a 460 nm/535 nm filter set for 2-NBDG imaging (Chroma
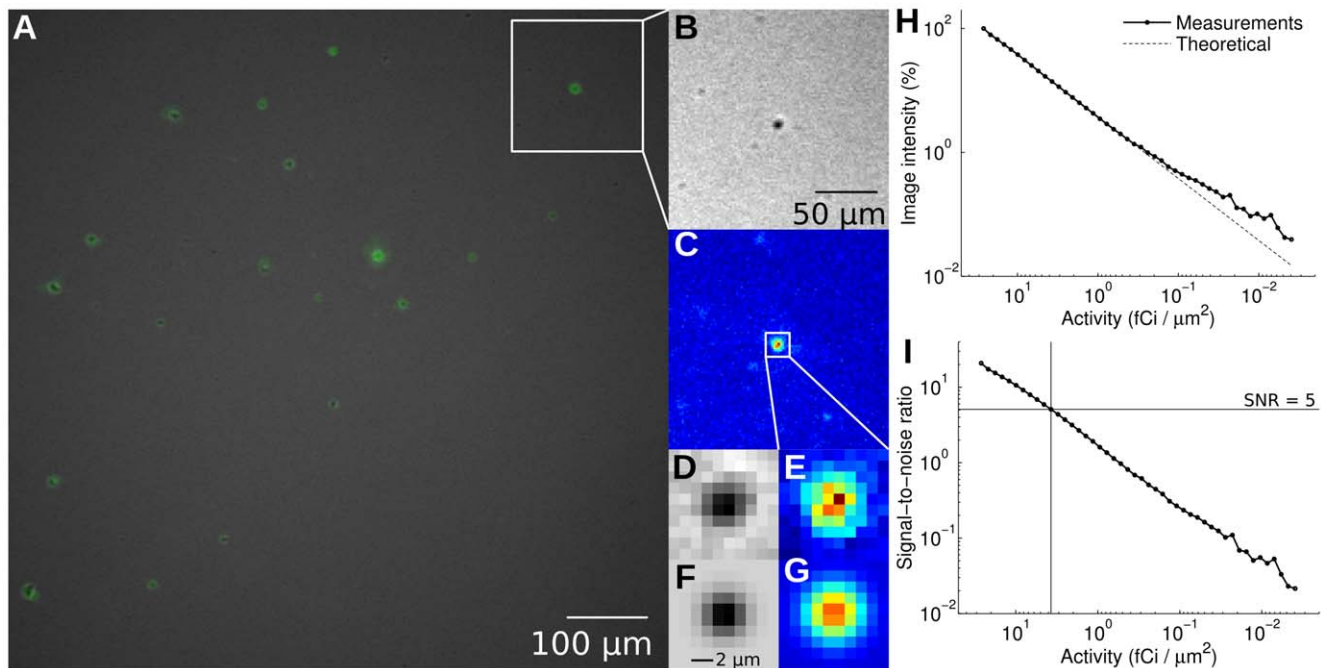
Figure 6. Performance characterization. FDG aggregates were obtained by evaporating an aqueous solution of FDG between a scintillator and a glass-bottom imaging dish. (**A**) Fused radioluminescence and brightfield images; (**B**) Brightfield and (**C**) radioluminescence images, magnified; (**D**) Brightfield and (**E**) radioluminescence images, further magnified, focusing on one particular FDG aggregate; (**F,G**) 2-D Gaussian fit of (D) and (E), respectively. (**H**) Radioluminescence microscope sensitivity, obtained by imaging the decay of a drop of FDG (2.6 µCi) over time. *Solid line*: mean pixel intensity; *Dashed line*: ideal exponential decay for ^{18}F. (**I**) Per-pixel signal-to-noise ratio, defined as the ratio of the average pixel intensity to the noise standard deviation. The sensitivity of the system is defined here as the amount of activity required per area to achieve a SNR of 5 (Rose criterion).
doi:10.1371/journal.pone.0046285.g006

Technology Corp., filter ref. D460/50x and D535/40 m) and a 540 nm/600 nm filter set for RFP imaging (Chroma Technology Corp., filter ref. HQ540/40x and HQ600/50 m).

Samples Preparation

MDA-MB-231 human breast cancer cells were purchased from the American Type Culture Collection (ATCC, Manassas, VA) and cultured in Leibovitz's L15 medium supplemented with 10% fetal bovine serum. One side of the scintillator plate was coated with fibronectin (10 µg/ml) to allow the cells to attach. After the plate had dried, the cells were seeded by placing a 50 µl drop containing 10^4 cells on the fibronectin-coated plate. Imaging was performed the following day.

PCR amplification and standard cloning techniques were used to insert the mrfp and ttk genes from plasmid pCDNA3.1-CMV-hrl-mrfp-ttk. A lentiviral EF1-gfp vector was purchased from System Biosciences (SBI, Mountain view, CA). The gfp fragment was removed from the vector and replaced with mrfp-ttk. For PCR amplification, different 5′ and 3′ end primers were used to generate the fusion vector (EF1-mrfp-ttk).

HeLa human cervical cancer and 293T human embryonic kidney cells were purchased from ATCC and cultured in high-glucose Dulbecco's modified eagle medium supplemented with 10% fetal bovine serum. 293T cells were used to produce the lentivirus following standard procedures. HeLa cells were transfected with concentrated lentivirus for 48 h, then trypsinized and seeded onto a scintillator plate coated with fibronectin (10 µg/ml) one day before imaging.

Imaging Protocol

For static imaging of glucose metabolism using combined fluorescence and radioluminescence microscopy, MDA-MB-231 cells were deprived of glucose in Leibovitz's L-15 medium 1 h before incubation with FDG (400 µCi) and 2-NBDG (Invitrogen, 100 µM). FDG was produced at the Stanford radiochemistry facility using an on-site cyclotron. Experiments were conducted shortly after synthesis of FDG to achieve high specific activity.

For dynamic imaging of glucose metabolism, three experiments were conducted: In the first experiment ("FDG"), MDA-MB-231 cells were deprived of glucose for 1 h, after which 5 µCi of FDG was added to their medium. Imaging started a few minutes later. In the second experiment ("FDG+glucose"), the same procedures were followed. Additionally, 25 mM of glucose was added to the medium at 2 h. In the third experiment ("FDG withdrawal"), the cells were preliminarily incubated in FDG (400 µCi, 1 h), and imaging started approximately 15 minutes after cell washing.

For imaging of transgene expression with FHBG and RFP, transfected HeLa cells were incubated for 2 h with 300 µCi of 18F-FHBG. The FHBG substrate was produced at the Stanford radiochemistry facility using an on-site cyclotron. To gather sufficient cell numbers, five fields were imaged at 40X using radioluminescence, fluorescence and brightfield microscopy. One field was also imaged with a 100X objective.

Image Corrections and Analysis

Image correction and analysis were performed using MATLAB R2010a (Mathworks, Natick, MA). Radioluminescence micrographs were corrected by subtraction of a dark image, taken with

the same exposure time but with a non-radioactive sample in the microscope. These images were further corrected for field flatness using a flat-field calibration map acquired using a uniform distribution of FDG. Gaussian filtering was applied where appropriate to reduce noise. During long exposures, high-energy photons (gamma rays and annihilation photons) interacted with the CCD and produced hot spots in the image. These hot spots were removed by applying a custom algorithm that can detect sharp features well above neighboring pixels. All radioluminescence images were corrected for radioactive decay. The timestamp of the first acquired image was used as the reference time point.

Fluorescence micrographs were corrected for background effects (filter bleed-through and camera dark noise) by subtracting a dark image taken with a non-fluorescent sample. Field flatness was corrected using a flat-field calibration map.

To measure radiotracer uptake in single cells, circular regions of interest (ROIs; diameter, 24 μm) were manually placed on the cells using the brightfield micrograph. Similar ROIs were placed in the background as controls. Cell radiotracer uptake was defined as the mean pixel intensity within the ROI of the corrected radioluminescence image. The same ROI analysis procedure was also applied to fluorescence micrographs.

The range of cell motion occurring during the exposure of a single frame is typically too small to result in any significant blurring. However, for extended timelapse imaging studies (1 h or longer), cell motion can no longer be neglected and must be accounted for when analyzing the images. We therefore manually placed circular ROIs on the each cell every 10 frames (i.e. every hour). In between these key frames, we assumed that the cells moved in a straight line.

Radiotracer Kinetic Modeling

Influx of FDG into glucose-deprived cells was described using the following two-tissue compartmental model:

$$\frac{C(t)}{C_a} = \frac{K_1 k_2}{(k_2 + k_3)^2}(1 - e^{-(k_2+k_3)t}) + \frac{K_1 k_3}{k_2 + k_3}t$$

where C_a is the extracellular FDG concentration (assumed to be fixed); $C(t)$ is the time-dependent intracellular FDG concentration (including free FDG and bound FDG-6-P); and K_1, k_2 and k_3 are the rate constants representing influx, efflux, and irreversible phosphorylation of FDG, respectively [23]. For $t > 1/(k_2 + k_3)$, the exponential term is becomes negligible. The intracellular and extracellular compartments are then in equilibrium, with the intracellular concentration of FDG rising linearly with time due to irreversible trapping. The slope and intercept of this linear rise are the Patlak coefficients [28]. We used non-linear weighted least-squares curve fitting to estimate the parameters of the model. The fitting weights were adjusted to decrease the contribution of later time points, which have higher noise due to radioactive decay.

Efflux of FDG from cells was modeled using a two-tissue compartmental model:

$$C(t) = a_1 e^{-\lambda_1 t} + a_2 e^{-\lambda_2 t}$$

where a_1 and a_2 are positive coefficients that depend on the initial conditions, and λ_1 and λ_2 are the eigenvalues of the differential system of equations describing transport of FDG between compartments. The rate constant k_4, which models the possible dephosphorylation of FDG-6-phosphate (FDG-6-P), was included in this model but assumed to be much smaller than k_3. Furthermore, due to the large extracellular volume (0.2 ml), the

concentration of FDG in the cell culture medium was assumed to remain negligible after withdrawal of FDG. Under these assumptions, the eigenvalues can be approximated as

$$\lambda_1 = k_2 + k_3 + \frac{k_2 k_4}{k_2 + k_3}$$

and

$$\lambda_2 = \frac{k_2 k_4}{k_2 + k_3}.$$

These rate parameters were estimated by fitting the efflux model to the measured time-activity curves. For cells for which the solution of the fit yielded $\lambda_1 \approx \lambda_2$ or $\lambda_2 < 1\,\mathrm{min}^{-1}$, the efflux curve was fitted with a single exponential function. In the special case of irreversible trapping ($k_4 = 0$), the model is described by a single exponential decay with rate $\lambda_1 = k_2 + k_3$.

Statistical Analysis

Correlation between fluorescence and radioluminescence ROI measurements was computed using the Pearson product-moment correlation coefficient. A p-value of less than 0.01 was considered statistically significant.

Spatial Resolution Characterization

To evaluate the performance of the radioluminescence microscope, we placed a drop of FDG (10 μCi) between the imaging dish and a scintillator plate. Upon evaporation of the aqueous solvent, FDG precipitated into small solid aggregates that could be seen both on brightfield and radioluminescence images. We measured the size of these aggregates by fitting them with 2-D Gaussian functions.

Sensitivity Characterization

The overall sensitivity of the system was evaluated by imaging the decay of a mixture of glycerol and FDG (2.6 μCi initially), placed between an imaging dish and a scintillator plate. Radioluminescence images were acquired every 31 min, using an EM gain of 251/1200 and an exposure time of 30 min. Within a large region of interest (370,000 pixels), pixel intensities were normalized to correct for field flatness using the first frame as a reference. The standard deviation of the noise, found to be Gaussian-distributed, was computed in each frame. The per-pixel signal to noise ratio was then defined as the ratio of the average pixel intensity to the standard deviation of the noise. The sensitivity of the system was defined as the activity (area density) required to achieve a signal-to-noise ratio of 5 (Rose criterion [26]).

Supporting Information

Video S1 Timelapse imaging of FDG influx kinetics in MDA-MB-231 cells using radioluminescence (*left*) and brightfield (*right*) microscopy. The cells were deprived of glucose one hour prior to imaging. Serial image acquisition was started after adding FDG (5 μCi) to the cell culture medium. (MP4)

Video S2 Timelapse imaging of competition between FDG and glucose uptake in MDA-MB-231 cells using

radioluminescence (*left*) and brightfield (*right*) micros-copy. The cells were deprived of glucose one hour prior to imaging. Serial image acquisition was started after adding FDG (5 µCi) to the cell culture medium. Additionally, 25 mM of glucose was added to the medium at 2 h.
(MP4)

Video S3   Timelapse imaging of FDG efflux kinetics in MDA-MB-231 cells using radioluminescence (*left*) and brightfield (*right*) microscopy. The cells were preliminarily incubated in FDG (400 µCi, 1 h), and imaging started approxi-mately 15 minutes after cell washing.
(MP4)

Author Contributions

Conceived and designed the experiments: GP PO LX. Performed the experiments: GP KC CS LM. Analyzed the data: GP CC. Wrote the paper: GP.

References

1. Yalow RS, Berson SA (1960) Immunoassay of endogenous plasma insulin in man. J Clin Invest 39: 1157–1175.
2. Phelps ME (2000) PET: The merging of biology and imaging into molecular imaging. J Nucl Med 41: 661–681.
3. Nordberg A, Rinne JO, Kadir A, Langstrom B (2010) The use of PET in Alzheimer disease. Nat Rev Neurol 6: 78–87.
4. Gambhir SS (2002) Molecular imaging of cancer with positron emission tomography. Nat Rev Cancer 2: 683–693.
5. Dobrucki LW, Sinusas AJ (2009) PET and SPECT in cardiovascular molecular imaging. Nat Rev Cardiol 7: 38–47.
6. Paltsyn AA, Tumanov VP, Serov GG (1990) Autoradiographic study of cell cultures. B Exp Biol Med 110: 1731–1734.
7. O'Brien RT, George LA (1959) Preparation of autoradiograms for electron microscopy. Nature 183: 1461–1462.
8. Johnston RF, Pickett SC, Barker DL (1990) Autoradiography using storage phosphor technology. Electrophoresis 11: 355–360.
9. Ott RJ, MacDonald J, Wells K (2000) The performance of a CCD digital autoradiography imaging system. Phys Med Biol 45: 2011–2027.
10. Mettivier G, Montesi MC, Russo P (2003) First images of a digital autoradiography system based on a Medipix2 hybrid silicon pixel detector. Phys Med Biol 48: 173–181.
11. Chen L, Gobar LS, Knowles NG, Liu Z, Gmitro AF, et al. (2008) Direct imaging of radionuclide-produced electrons and positrons with an ultrathin phosphor. J Nucl Med 49: 1141–1145.
12. Kanno S, Rai H, Ohya T, Hayashi Y, Tanoi K, et al. (2007) Real-time imaging of radioisotope labeled compounds in a living plant. J Radioanal Nucl 272: 565–570.
13. Charpak G, Dominik W, Zaganidis N (1989) Optical imaging of the spatial distribution of beta-particles emerging from surfaces. Proc Natl Acad Sci USA 86: 1741–1745.
14. Cairns RA, Harris IS, Mak TW (2011) Regulation of cancer cell metabolism. Nature Rev Cancer 11: 85–95.
15. Jadvar H, Alavi A, Gambhir S (2009) 18F-FDG uptake in lung, breast, and colon cancers: Molecular biology correlates and disease characterization. J Nucl Med 50: 1829–1827.
16. Reivich M, Kuhl D, Wolf A, Greenberg J, Phelps M, et al. (1979) The [18F] fluorodeoxyglucose method for the measurement of local cerebral glucose utilization in man. Circ Res 44: 127–137.
17. Heimberg H, De Vos A, Vandercammen A, Van Schaftingen E, Pipeleers D, et al. (1993) Heterogeneity in glucose sensitivity among pancreatic beta-cells is correlated to differences in glucose phosphorylation rather than glucose transport. EMBO J 12: 2873–2879.
18. Pugachev A, Ruan S, Carlin S, Larson SM, Campa J, et al. (2005) Dependence of FDG uptake on tumor microenvironment. Int J Radiat Oncol 62: 545–553.
19. Yoshioka K, Takahashi H, Homma T, Saito M, Oh KB, et al. (1996) A novel fluorescent derivative of glucose applicable to the assessment of glucose uptake activity of Escherichia coli. Biochim Biophys Acta 1289: 5–9.
20. Yamada K, Saito M, Matsuoka H, Inagaki N (2007) A real-time method of imaging glucose uptake in single, living mammalian cells. Nature Protoc 2: 753–762.
21. Tseng JC, Wang Y, Banerjee P, Kung A (2012) Incongruity of imaging using fluorescent 2-DG conjugates compared to 18F-FDG in preclinical cancer models. Mol Imaging Biol (in press).
22. Yoshioka K, Saito M, Oh K, Nemoto Y, Matsuoka H, et al. (1996) Intracellular fate of 2-NBDG, a fluorescent probe for glucose uptake activity, in Escherichia coli cells. Biosci Biotech Biochem 60: 1899–1901.
23. Carson RE (2005) Tracer Kinetic Modeling in PET. In: Bailey DL, Townsend DW, Valk PE, Maisey MN, editors. Positron Emission Tomography. London: Springer. 127–159.
24. Ray P, De A, Min JJ, Tsien RY, Gambhir SS (2004) Imaging tri-fusion multimodality reporter gene expression in living subjects. Cancer Res 64: 1323.
25. Yaghoubi S, Barrio JR, Dahlbom M, Iyer M, Namavari M, et al. (2001) Human pharmacokinetic and dosimetry studies of [18F] FHBG: a reporter probe for imaging herpes simplex virus type-1 thymidine kinase reporter gene expression. J Nucl Sc. 42: 1225–1234.
26. Leidholdt EM, Bushberg JT, Seibert JA, Boone JM (2006) The essential physics of medical imaging 2nd edn. Philadelphia:Lippincott Williams & Wilkins.
27. Ensley J, Maciorowski Z, Pietraszkiewicz H, Hassan M, Kish J, et al. (1987) Solid tumor preparation for clinical application of flow cytometry. Cytometry A 8: 488–493.
28. Patlak CS, Blasberg RG, Fenstermacher JD (1983) Graphical evaluation of blood-to-brain transfer constants from multiple-time uptake data. J Cerebr Blood F Met 1: 1–7.

Intraoperative Imaging of Tumors Using Cerenkov Luminescence Endoscopy: A Feasibility Experimental Study

Hongguang Liu*[1], Colin M. Carpenter*[2], Han Jiang[1], Guillem Pratx[2], Conroy Sun[2], Michael P. Buchin[3], Sanjiv S. Gambhir[1,4], Lei Xing[2], and Zhen Cheng[1]

[1]*Molecular Imaging Program at Stanford (MIPS), Department of Radiology and Bio-X Program, Canary Center at Stanford for Cancer Early Detection, Stanford University, Stanford, California;* [2]*Department of Radiation Oncology, Stanford University, Stanford, California;* [3]*Stanford Photonics, Inc., Palo Alto, California; and* [4]*Department of Bioengineering and Materials Science and Engineering, Stanford University, Stanford, California*

Cerenkov luminescence imaging (CLI) is an emerging new molecular imaging modality that is relatively inexpensive, easy to use, and has high throughput. CLI can image clinically available PET and SPECT probes using optical instrumentation. Cerenkov luminescence endoscopy (CLE) is one of the most intriguing applications that promise potential clinical translation. We developed a prototype customized fiberscopic Cerenkov imaging system to investigate the potential in guiding minimally invasive surgical resection. **Methods:** All experiments were performed in a dark chamber. Cerenkov luminescence from ^{18}F-FDG samples containing decaying radioactivity was transmitted through an optical fiber bundle and imaged by an intensified charge-coupled device camera. Phantoms filled with ^{18}F-FDG were used to assess the imaging spatial resolution. Finally, mice bearing subcutaneous C6 glioma cells were injected intravenously with ^{18}F-FDG to determine the feasibility of in vivo imaging. The tumor tissues were exposed, and CLI was performed on the mouse before and after surgical removal of the tumor using the fiber-based imaging system and compared with a commercial optical imaging system. **Results:** The sensitivity of this particular setup was approximately 45 kBq (1.21 μCi)/300 μL. The 3 smallest sets of cylindric holes in a commercial SPECT phantom were identifiable via this system, demonstrating that the system has a resolution better than 1.2 mm. Finally, the in vivo tumor imaging study demonstrated the feasibility of using CLI to guide the resection of tumor tissues. **Conclusion:** This proof-of-concept study explored the feasibility of using fiber-based CLE for the detection of tumor tissue in vivo for guided surgery. With further improvements of the imaging sensitivity and spatial resolution of the current system, CLE may have a significant application in the clinical setting in the near future.

Cerenkov luminescence imaging (CLI) has recently attracted increasing interest in the field of molecular imaging (*1,2*). CLI is a new optical imaging modality in which images are obtained by monitoring the Cerenkov photons emitted from highly energetic moving charged particles (β$^+$ or β$^-$). Conventional nuclear imaging methods, such as PET and SPECT, are the most widely used clinical molecular imaging techniques. However, these modalities usually suffer from high cost, limited availability, relatively low spatial resolution, and low throughput (*3*). As a technique that bridges optical imaging and radionuclide imaging, CLI has shown many advantages such as high sensitivity, high resolution, low cost, wide availability, relatively high throughput, and commercially available radionuclide probes already approved by the Food and Drug Administration.

Since its discovery in 2009, CLI has quickly become a practical molecular imaging technique, and many new applications of CLI in preclinical research continue to emerge (*1,2*). Several research groups have demonstrated that CLI can be a powerful tool for tumor imaging using radionuclide probes such as ^{18}F-FDG. Important validation studies have also been performed, and it was reported that there is a good linear correlation between the tumor uptake quantified by PET and tumor CLI signals in subcutaneous xenograft models (*4–7*). CLI has also been found to be useful for imaging α and pure β$^-$ emitters such as ^{90}Y and ^{225}Ac, which are used for cancer treatment (*4*). Moreover, CLI can be applied in the monitoring of reporter gene expression. The herpes simplex virus type 1 thymidine kinase and the sodium iodide symporter reporter genes were recently successfully imaged by CLI in conjunction with

appropriate radioactive reporter probes (4,8,9). Cerenkov photons have also been used to illuminate fluorescent dyes and nanoparticles for in vivo imaging (10–13). A recent study further showed that CLI could be used for monitoring tumor surgery in xenograft mouse models, highlighting the translational potential of the modality (14). CLI has also been used to measure the radiochemical purity of a radiolabeled compound and to image plant physiology (15). In addition to these applications, the recent advancement in CLI tomography makes this novel imaging modality even more powerful and promising for biomedical research including diagnostic imaging and therapeutic monitoring (16–19).

Because it can image clinically available radiotracers, CLI has the potential to be rapidly translated into clinical applications (4,18). However, all the studies described above have involved the use of conventional small-animal optical imaging systems, which are not compatible with routine clinical practice. In this study, we have built the first, to our knowledge, prototype system that is amenable to Cerenkov luminescence endoscopy (CLE) in the clinic. This system comprises an optical fiber bundle and an intensified charge-coupled device (CCD) camera. The small-diameter flexible endoscope is designed for minimally invasive monitoring of living tissues and organs, using a sensitive camera to produce images of the radionuclide probe. It is also expected that hollow organs (e.g., bladder and lung) or insufflated cavities (e.g., esophagus and colon) inside the body can provide natural and anatomic dark chambers for CLE. By overlaying conventional bright-field images commonly obtained from an endoscope with the Cerenkov luminescence images generated by radionuclide probes, CLE could be used to identify diseased tissues for diagnostic purposes and real-time monitoring of endoscopic surgery.

Therefore, we investigated the feasibility of CLE for guiding cancer surgical resection by performing sensitivity, spatial-resolution, and proof-of-concept experiments. The characteristic sensitivity of this system was evaluated using the natural decay of ^{18}F-FDG. Imaging resolution was determined using a phantom with cylindric holes. Finally, imaging studies were performed to demonstrate surgical guidance in a small-animal tumor model. A well-known commercial optical imaging system was used to provide a comparison. The data presented herein outline the instrumentation and methodology; further steps that are needed to translate this modality into the clinic are also discussed.

MATERIALS AND METHODS

^{18}F-FDG was produced by the Radiochemistry Facility at Stanford University. The rat glioma cell line C6 was obtained from American Type Culture Collection. Female athymic nude mice (nu/nu) (n = 5) obtained from Charles River Laboratories, Inc., were 4–6 wk old. A CRC-15R PET dose calibrator (Capintec Inc.) was used for all radioactivity measurements.

Tumor Model

All animal studies were performed in compliance with federal and local institutional guidelines for the conduct of animal experimentation. C6 cells were cultured in Dulbecco modified Eagle medium supplemented with 10% fetal bovine serum and 1% penicillin/streptomycin (Invitrogen Life Technologies). The cell line was maintained in a humidified atmosphere of 5% CO_2 at 37°C, with the medium changed every other day. A 75% confluent monolayer was detached with trypsin and dissociated into a single-cell suspension for further cell culture. Approximately 1×10^6 C6 cells suspended in phosphate-buffered saline (0.1 M, pH 7.2; Invitrogen) were implanted subcutaneously in the left legs of nude mice. Tumors were allowed to grow to 150–200 mm^3 (2–3 wk), and the tumor-bearing mice were imaged in vivo.

CLI

Validation CLI was performed with an IVIS Spectrum system (Caliper Life Sciences). For all in vivo studies, radionuclides were diluted in phosphate-buffered saline. Animals were placed in a light-tight chamber under isoflurane anesthesia. Each acquisition took 3 min for all studies without filters. Images were acquired and analyzed using Living Image 3.0 software (Caliper Life Sciences). The mice were kept fasting overnight before ^{18}F-FDG imaging and anesthetized by inhalation of 2% isoflurane during the experiment.

Fiber-Based CLE System

The fiber-based CLE system used an imaging optical fiber coupled to a highly sensitive intensified CCD camera. The application of this system for surgical oncology guidance is detailed in Figure 1. Specifically, a microimaging lens (Cinegon, F/1.4, 12-mm focal length; Schneider) was coupled at the distal end of an optical imaging fiber bundle that was 108 mm long, with a 5 × 6.7 mm active area. The pixels of the fiber bundle are made of discrete 10-µm fibers (IG154; Schott). At the proximal end, a Pentax (F/1.4) lens provided relay optics to the camera (Supplemental Fig. 1A; supplemental materials are available online only at http://jnm.snmjournals.org). The camera, an image-intensified
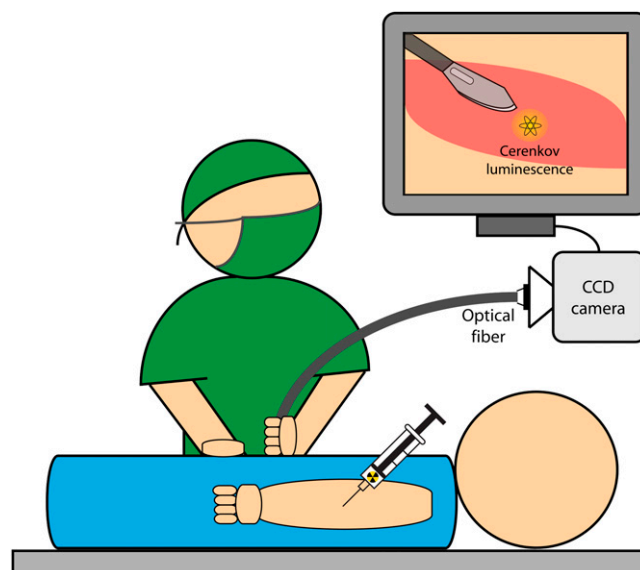

FIGURE 1. Suggested application of fiber-based system for endoscopic and laparoscopic CLI.

CCD (Turbo 640-Z; Stanford Photonics Inc.), had 640 × 480 pixels and single-photon imaging capability (Supplemental Fig. 1B). To minimize background light and to emulate a light-tight anatomic cavity, all images were taken in a dark box. In addition, images were postprocessed with a software thresholding technique that removed pixel values below a manufacturer-recommended value; this optimal value was chosen to remove low-intensity pixels that corresponded to thermal and read noise on the CCD. These steps reduced the noise to approximately 20 counts per second.

Imaging Using Fiber-Based System

Images were acquired at a high frame-rate of 120 Hz to allow for maximal reduction in noise. The noise-reduction step described above was performed for each frame. These frames were then accumulated for 5 min to form the raw data. The raw data were image-processed offline using an algorithm to remove cosmic and stray γ-events. This algorithm removed noisy pixels by thresholding the gradient around each pixel in its local area. An additional denoising step removed spurious bright pixels that appeared in sequential exposures.

The fiber-based CLE system was characterized for sensitivity by imaging 2 adjacent wells of a black 96-well plate (300 μL per well). A glycerol and water mixture combined with 3.7 MBq (100 μCi) of ^{18}F-FDG was in 1 well, and a glycerol and water mixture only was in a nearby well. Images were sequentially acquired over approximately 10 half-lives (19 h, 43 min), and each data point was formed from 5 min of photon accumulation.

The spatial resolution of the system was characterized using a standard PET/SPECT phantom (Micro Hot-Spot Phantom; Data Spectrum Corp.) filled with 15.2 MBq (410 μCi) of ^{18}F-FDG; this phantom is also commonly used to evaluate the spatial resolution of PET systems. Both the 2.4- and the 1.6-mm cylindric holes were used to form line profiles, taken from the fiber-based images. An ambient-light image and a functional Cerenkov luminescence image were acquired. The exposure time for all ambient images was less than 1 s, and the functional image acquisition time was 5 min. The subject was 5 cm from the optical system.

Fiber-Based CLE System for Surgery Monitoring

Five mice were injected with 37 MBq (1 mCi) of ^{18}F-FDG via the tail vein. The tracer was allowed to accumulate for 60–70 min, and the mice were imaged in the IVIS system to verify tumor uptake of ^{18}F-FDG. Tumors were then imaged with the IVIS and fiber-based CLE systems after removal of the skin covering the subcutaneous tumor and after excision of the tumor. To simulate an environment mimicking surgical resection, and to validate the origin of the signal, the excised tumor was also imaged after being placed adjacent to the surgical cavity. Two images were acquired for each of these steps: 1 ambient image and 1 functional Cerenkov luminescence image. The exposure time for all ambient images was less than 1 s, and the functional image acquisition time was 5 min.

Statistical Methods

Quantitative data were expressed as mean ± SD. Means were compared using the Student t test. A 95% confidence level was chosen to determine the significance between groups, with P values of less than 0.05 indicating significant differences.
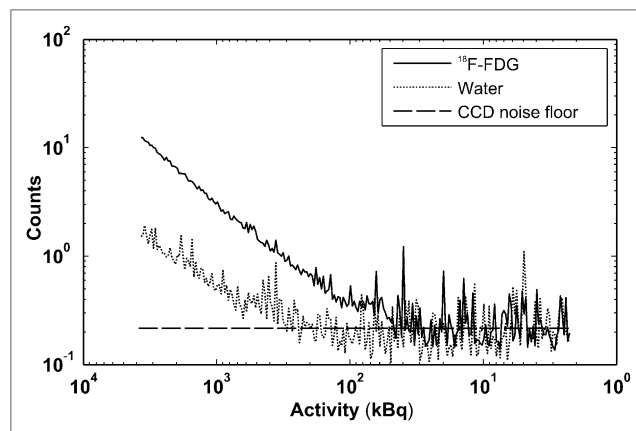

FIGURE 2. System sensitivity via sequential imaging of 3.7 MBq (100 μCi) of ^{18}F-FDG for approximately 20 h. Optical signals from ^{18}F-FDG and control sample were plotted.

RESULTS

System Characterization

Figure 2 shows the reduction in signal during ^{18}F-FDG decay over time for 2 wells: 1 filled with ^{18}F-FDG and 1 filled with a water and glycerol mixture only. With a 5-min integration time, a minimum of approximately 45 kBq (1.21 μCi) of activity can be identified as different from the control well containing the water and glycerol solution (signal-to-noise ratio > 1). There was a decrease in signal in the control well due to stray γ-photons from the ^{18}F-FDG well interacting with the optical fiber and creating scintillation background light in the image.
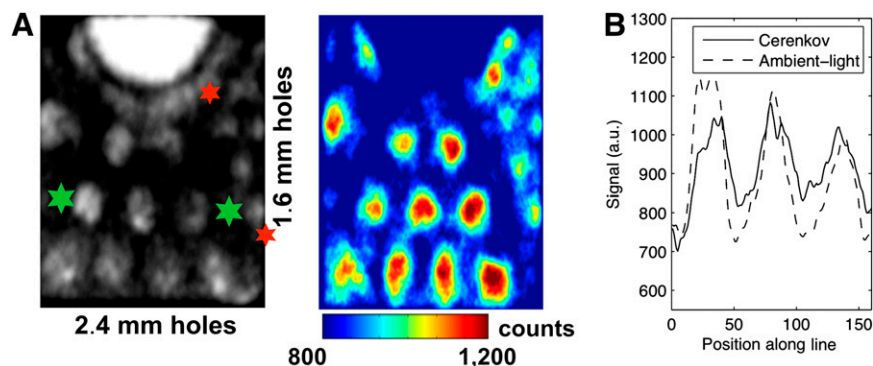
Visually, the photographic and Cerenkov images taken using the standard IVIS imaging system (Supplemental Fig. 2) are similar to the photographic and Cerenkov images taken with the fiber-based system (Fig. 3A). The line profiles demonstrate a high correlation between the Cerenkov and photographic line profiles. For the 2.4-mm holes (Fig. 3B), the line profile limits depicted by the large green stars in Figure 3A had a Pearson correlation coefficient of 0.78 (significance, $P < 1e-5$). For the 1.6-mm holes (Supplemental Fig. 3), the line profile limits depicted by the smaller red stars had a Pearson correlation coefficient of 0.71 (significance, $P < 1e-5$). The peaks were also in near-identical locations; the difference in peak locations between the holes for the line profiles of the photographic and Cerenkov-emission images was 3.8%, a difference of only a few pixels.

System Demonstration

The images comparing both systems before removal of the tumor for mouse 1 are shown in Figure 4 (IVIS system [Fig. 4A] and fiber-based CLE system [Fig. 4B]). Figure 5A shows the images produced by the IVIS system, and Figure 5B shows images from the fiber-based CLE system after removal of the tumor in mouse 1.

Comparing images in Figure 5B quantitatively, we determined the tumor-to-background ratio for the Cerenkov signal by computing the ratio of the median value in the

FIGURE 3. Characterization of fiberscopic system spatial resolution. (A) Respective ambient (left) and Cerenkov images (right) of PET/SPECT phantom (4.3-cm inner diameter). (B) Quantitative line profiles of ambient and Cerenkov images for 2.4-mm holes; line sampled is indicated by green stars in A. a.u. = arbitrary units.

region of interest encircling the excised tumor to the median value in the cleared tumor cavity. This ratio was 1.28 (for comparison, the tumor-to-background ratio from the IVIS system was 1.16 for the 3-min scan). For mice 2, 3, 4, and 5, the tumor-to-background ratios for the removed tumor were 1.41, 1.21, 1.02, and 1.17, respectively. Tumor tissue light emission was significantly higher than the exposed cavity for all mice (Student t test for paired samples, $P < 0.05$ for all). Much of the low tumor-to-background value in mouse 4 can be explained by the reflection of the light emitted from the tumor by the tumor cavity, which was directly adjacent. Residual tumor tissue after surgery is also possible.

DISCUSSION

In this study, we demonstrated the methodology and performance of an optical fiber system built to image tumor margins during surgical resection. Cerenkov imaging has been proposed for small-animal drug discovery and surgical guidance, yet previous studies have used an imaging box with a lens-mounted imaging system; this setup is not realistic for subjects that are larger (e.g., large animals and humans). We recently demonstrated the feasibility of endoscopic imaging of Cerenkov light using conventional optical fiber bundle/clinical endoscopes, an optical imaging lens system, and a sensitive low-noise CCD camera (20). Hereby, for the first time we investigated a Cerenkov endoscope for surgical resection. We have shown that this system is capable of imaging 1.2-mm structures, using phantom experiments. We determined the sensitivity of the system for ^{18}F-FDG (~45 kBq [1.21 μCi]/300 μL). We then demonstrated the ability to visualize the accumulation of ^{18}F-FDG in a tumor using this system and could track the contrast as the tumor was excised from the mouse.

A benefit of a Cerenkov endoscope is that it provides higher image spatial resolution than PET and SPECT cameras, because the optical photons emitted from the tissue surface are detected with optical lenses and a high-resolution CCD chip. Cho et al. demonstrated a limit of 350 μm (in full width at half maximum) with a system designed for visualizing a microfluidic chip setup (21). This resolution is affected by the imaging system, the range of the β-particles in the tissue, and tissue optical

scatter. Levin and Hoffman showed that the mean β-particle track of ^{18}F-FDG had a full width at half maximum value of 102 μm in water (22), which determines the physical resolution limit of a Cerenkov scope when imaging ^{18}F-FDG. Improved resolution may be achieved using a radioisotope with a β-particle decay of lower energy, such as ^{131}I, although this would result in lower sensitivity because there is an inverse relationship between resolution and sensitivity. We do note some inconsistency in the image of the 1.2-mm holes, but many of these holes are clearly visualized. The high spatial resolution of the system requires accurate focus of the optics both at the distal fiber–lens junction and at the proximal fiber–camera junction—an optical focus that will be improved in our further
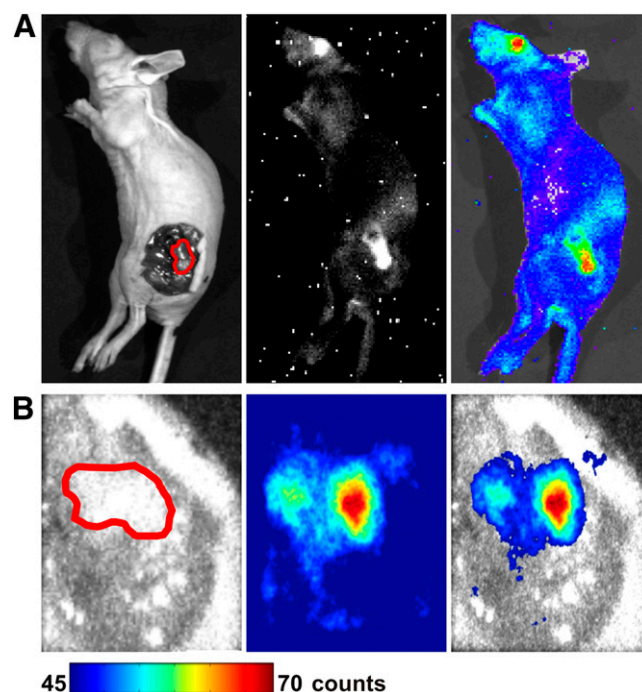

FIGURE 4. Mouse 1 bearing C6 glioma after tail-vein administration of 37 MBq (1 mCi) of ^{18}F-FDG. (A) Mouse was imaged by commercially available optical IVIS system, and images were compared with those from prototype fiber-based system (B). Tumor tissues are outlined by red lines. Ambient-light images are on left, luminescent images are in middle, and fused images are on right.
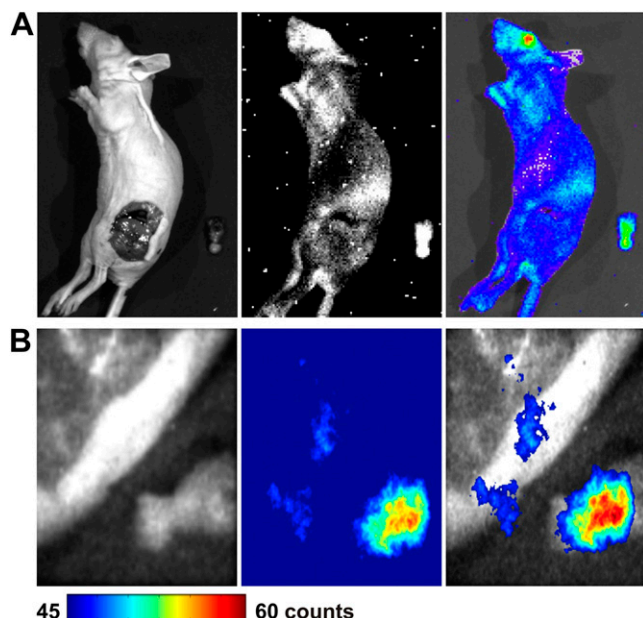
FIGURE 5. Mouse 1 was imaged by IVIS optical system (A) and fiber-based system (B) after surgery to remove tumor tissues. Ambient-light images are on left, luminescent images are in middle, and fused images are on right.

studies. In the case of our phantom, the resolution of the Cerenkov luminescence images was also degraded by reflections within the translucent phantom and the signal-to-noise ratio of the single-photon–counting camera, which was not entirely optimized. The signal-to-noise ratio of our ambient-light image was also affected by a slightly imperfect focus and the suboptimal settings of the illumination source and camera. Thus, although we demonstrated the ability to visualize many of these 1.2-mm cylindric holes in a phantom with this endoscope-based system, we expect to be able to image submillimeter lesions with a more optimized system.

The sensitivity limit of this system was 45 kBq (1.2 μCi)/300 μL with ^{18}F-FDG. To put this in a practical perspective, if this system were used for head and neck tumors of the oropharynx (with a standardized uptake value of 5.17), 2.1 GBq (54 mCi) would have to be injected intravenously into a 70-kg patient to have enough activity to visualize a 300-μg tumor (*23*) in a 5-min scan; a more sensitive scope would enable the identification of smaller structures or similar structures with a reduction in ionizing dose to the patient and clinical staff. Increased sensitivity may be realized with more sensitive optics (such as an F/0.95 lens) or fiber optic glass, which transmits farther into the violet and ultraviolet emissions. The fiberglass used in this experiment was Schott-75 glass, which transmits 40% light at 500 nm; thus, it is not optimized for detecting the short-wavelength–dominant Cerenkov emission. In addition, γ-photons emitted from the radiotracer scintillate impurities in the glass, resulting in undesired background noise. The use of fused silica, which is much more sensitive

to the ultraviolet and violet emissions and has fewer impurities, would improve sensitivity.

As a prototype device, the off-the-shelf optical lens on this system was too large (3-cm diameter) for many endoscopic or laparoscopic applications. However, smaller custom optics could be designed to enable imaging through smaller apertures. Meanwhile, optimized optic lenses and fibers can provide better sensitivity and shorter integration time in upcoming systems. We leave this investigation for future studies using more customized optical systems.

The main advantage of this system over other optical techniques, such as fluorescence imaging, is that it is able to use standard PET tracers, such as ^{18}F-FDG, which are already available in the clinic. Many novel tracers such as 3′-deoxy-3′-^{18}F-fluorothymidine, engineered proteins, and labeled arginine-glycine-aspartic acid peptides are in the pipeline of clinical trials required by the Food and Drug Administration because of their utility in PET. This is a significant advantage for this technique, because much effort and innovation is being dedicated to PET tracers. In contrast, because of the lack of a standardized imaging device for optical imaging, optical contrast agents are not being sufficiently developed to keep pace with radiotracers. Thus, the main advantage of a Cerenkov emission surgical scope is that it is readily clinically translatable. The combination of PET and Cerenkov imaging provides an opportunity to use an identical signal origin, and perhaps an identical injection, to localize tumors for excision.

CONCLUSION

This proof-of-concept study demonstrated the feasibility of using fiber-based CLE for the detection of tumor tissue in vivo and demonstrated its potential use for image-guided surgery. With further improvement in imaging sensitivity and resolution of the current system, it is expected that Cerenkov imaging might soon be translated into clinical applications.

DISCLOSURE STATEMENT

The costs of publication of this article were defrayed in part by the payment of page charges. Therefore, and solely to indicate this fact, this article is hereby marked "advertisement" in accordance with 18 USC section 1734.

REFERENCES

1. Xu Y, Liu H, Cheng Z. Harnessing the power of radionuclides for optical imaging: Cerenkov luminescence imaging. *J Nucl Med.* 2011;52:2009–2018.

2. Lucignani G. Cerenkov radioactive optical imaging: a promising new strategy. *Eur J Nucl Med Mol Imaging.* 2011;38:592–595.

3. Massoud TF, Gambhir SS. Molecular imaging in living subjects: seeing fundamental biological processes in a new light. *Genes Dev.* 2003;17:545–580.

4. Liu H, Ren G, Miao Z, et al. Molecular optical imaging with radioactive probes. *PLoS ONE.* 2010;5:e9470.

5. Robertson R, Germanos MS, Li C, Mitchell GS, Cherry SR, Silva MD. Optical imaging of Cerenkov light generation from positron-emitting radiotracers. *Phys Med Biol.* 2009;54:N355-365.

6. Boschi F, Calderan L, D'Ambrosio D, et al. In vivo ^{18}F-FDG tumour uptake measurements in small animals using Cerenkov radiation. *Eur J Nucl Med Mol Imaging.* 2011;38:120–127.

7. Ruggiero A, Holland JP, Lewis JS, Grimm J. Cerenkov luminescence imaging of medical isotopes. *J Nucl Med.* 2010;51:1123–1130.

8. Liu H, Ren G, Liu S, et al. Optical imaging of reporter gene expression using a positron-emission-tomography probe. *J Biomed Opt.* 2010;15:060505.

9. Jeong SY, Hwang MH, Kim JE, et al. Combined Cerenkov luminescence and nuclear imaging of radioiodine in the thyroid gland and thyroid cancer cells expressing sodium iodide symporter: initial feasibility study. *Endocr J.* 2011;58:575–583.

10. Liu H, Zhang XF, Xing BG, Han PZ, Gambhir SS, Cheng Z. Radiation-luminescence-excited quantum dots for in vivo multiplexed optical imaging. *Small.* 2010;6:1087–1091.

11. Dothager RS, Goiffon RJ, Jackson E, Harpstrite S, Piwnica-Worms D. Cerenkov radiation energy transfer (CRET) imaging: a novel method for optical imaging of PET isotopes in biological systems. *PLoS ONE.* 2010;5:e13300.

12. Lewis MA, Kodibagkar VD, Oz OK, Mason RP. On the potential for molecular imaging with Cerenkov luminescence. *Opt Lett.* 2010;35:3889–3891.

13. Sun C, Pratx G, Carpenter CM, et al. Synthesis and radioluminescence of PE-Gylated Eu(3+)-doped nanophosphors as bioimaging probes. *Adv Mater.* 2011;23:H195–H199.

14. Holland JP, Normand G, Ruggiero A, Lewis JS, Grimm J. Intraoperative imaging of positron emission tomographic radiotracers using Cerenkov luminescence emissions. *Mol Imaging.* 2011;10:177–186.

15. Park JC, An GI, Park SI, et al. Luminescence imaging using radionuclides: a potential application in molecular imaging. *Nucl Med Biol.* 2011;38:321–329.

16. Hu Z, Liang J, Yang W, et al. Experimental Cerenkov luminescence tomography of the mouse model with SPECT imaging validation. *Opt Express.* 2010;18:24441–24450.

17. Li C, Mitchell GS, Cherry SR. Cerenkov luminescence tomography for small-animal imaging. *Opt Lett.* 2010;35:1109–1111.

18. Spinelli AE, Kuo C, Rice BW, et al. Multispectral Cerenkov luminescence tomography for small animal optical imaging. *Opt Express.* 2011;19:12605–12618.

19. Xu Y, Chang E, Liu H, Jiang H, Gambhir SS, Cheng Z. Proof-of-concept study of monitoring cancer drug therapy with Cerenkov luminescence imaging. *J Nucl Med.* 2012;53:312–317.

20. Kothapalli SR, Liu H, Liao JC, Cheng Z, Gambhir SS. Endoscopic imaging of Cerenkov luminescence. *Biomed Opt Express.* 2012;3:1215–1225.

21. Cho JS, Taschereau R, Olma S, et al. Cerenkov radiation imaging as a method for quantitative measurements of beta particles in a microfluidic chip. *Phys Med Biol.* 2009;54:6757–6771.

22. Levin CS, Hoffman EJ. Calculation of positron range and its effect on the fundamental limit of positron emission tomography system spatial resolution. *Phys Med Biol.* 1999;44:781–799.

23. Allal AS, Slosman DO, Kebdani T, Allaoua M, Lehmann W, Dulguerov P. Prediction of outcome in head-and-neck cancer patients using the standardized uptake value of 2-[18f]fluoro-2-deoxy-d-glucose. *Int J Radiat Oncol Biol Phys.* 2004;59:1295–1300.